To my mother,

And to all my friends in Montréal

Abstract

The effects of austenite grain size, level of undercooling, and strain and strain rate in compression on the austenite-to-ferrite transformation in a 0.1% C, 1.4% Mn steel were investigated. The influence of this transformation on the hot ductility of the steel in question was then examined. Samples were strained at rates from 3×10^{-4} s^{-1} to 3×10^{-2} s^{-1} after cooling to holding temperatures between the Ae_3 and the (undeformed) Ar_3 temperature.

Deformation was found to raise the effective Ar_3 temperature almost to the Ae_3, and to significantly accelerate the transformation in both fine (~ 25 μm) and coarse (~ 200 μm) grained samples. At relatively small levels of undercooling (~ 40°C), it was found that deformation induced ferrite could not form outside the regions of the material that were significantly affected by the applied strain. At low strain rates and in coarse grained material, this meant that ferrite formed in narrow bands near the grain boundaries. No such restriction was found in fine grained material.

In tension, it was found that, if thin bands of grain boundary ferrite were present in the microstructure, failure always occurred in this second phase. The effect of intergranular ferrite on the ductility was found to vary with the amount present; the lowest %RA value was obtained with around 10% ferrite present in the microstructure. The detrimental effect of ferrite lessened slightly as the strain rate was raised.

It is concluded that, from an industrial perspective, unless unbending can be performed at strain rates in excess of 3×10^{-2} s^{-1}, it would be prudent to carry out this operation either above the Ae_3 or below the (undeformed) Ar_3 temperature for the steel in question.

Résumé

Les effets de la taille de grain austénitique, de la chute en température en dessous de Ae_3, de la déformation et de la vitesse de déformation sur la transformation de l'austénite en ferrite ont été étudiés pour un acier contenant 0.1% C et 1.4% Mn. L'influence de cette transformation sur la ductilité à chaud de cet acier a également été mis en évidence. Les échantillons utilisés furent déformés à des vitesses allant de 3×10^{-4} s^{-1} à 3×10^{-2} s^{-1}, après refroidissement jusqu'à des températures situées entre Ae_3 et Ar_3 (sans déformation).

Il s'est avéré que la déformation appliquée a entraîné une élévation de la température d'arrêt Ar_3, et ce quasiment jusqu'à la température d'équilibre Ae_3, ainsi qu'une accélération de la transformation, à la fois dans les échantillons possédant une petite taille de grain (~ 25 μm) et dans ceux possédant une taille de grain plus importante (~ 200 μm). Pour de faibles chutes de température sous Ae_3 (~ 40°C), la phase ferritique résultant de la transformation induite par la déformation appliquée ne pouvait pas se former à l'extérieur des zones qui furent déformées de maniére significative. Ainsi, pour des vitesses de déformation faibles et pour des échantillons composés de gros grains, la ferrite ne s'est formée que dans des bandes proches des joints de grains. Un phénomène semblable ne fut pas observé dans les échantillons composés de petits grains.

De plus, pour les échantillons comportant de telles bandes, la rupture lors de tests de traction a, à chaque fois, été observée à l'intérieur de celles-ci. Par ailleurs, il est apparu que la quantité de ferrite présente entre les grains affecte la ductilité: la plus petite valeur de %RA (reduction aréolaire en pourcents) a été observée pour une quantité de ferrite de 10%, l'effet négatif de cette ferrite diminuant avec l'augmentation de la vitesse de déformation.

En conclusion, d'un point de vue industriel, à moins que le redressement ne soit fait à une vitesse de déformation excédant 3×10^{-2} s^{-1}, il serait plus prudent d'effectuer cette opération à une température supérieure à Ae_3 ou inférieure à Ar_3 (sans déformation) pour l'acier en question.

Acknowledgements

I would like to express my gratitude to Professor John J. Jonas for giving me the opportunity to work under him in the CSIRA steel processing laboratories at McGill University, and for the invaluable instruction and example that he has provided. I would also like to convey my sincere thanks to Professor Barrie Mintz of the City University, London, England for his help and guidance over the past several years, and for the constant encouragement that both he and Mrs. Jenny Mintz have been kind enough to offer me during this time.

I feel that I have benefited greatly from the warm, friendly atmosphere that exists within the Jonas/Yue group, and from the exemplary spirit of the researchers, graduate students and ancillary staff that work under its auspices. I am personally indebted to quite a number of the aforementioned, and would particularly like to thank certain of them. Firstly, I would like to acknowledge my office mates, particularly Matthew Barnett, Jerzy Baczynski, Ian De Ardo and Leo Kestens; for outstanding company and camaraderie and for the many enlightening discussions that we have had. Secondly I would like to thank Edwin Fernandez and Terry Maccagno, for their untiring patience in helping me to prepare my specimens and to modify equipment. Thirdly, I would like to convey my appreciation to Lorraine Mello, for making some sense of the administrative nightmare that lurks beneath the surface of any university. Finally, I would like to mention Joseph Azar, who so ably translated my Abstract into French.

Perhaps most importantly, I would like to thank my mother, without whose selfless generosity and unconditional support none of this would have been possible.

Table of Contents

List of Figures

List of Tables

Chapter 1

Introduction

Over the past three decades, continuous casting has become the premier casting route used in making semi-finished steel products, replacing the traditional ingot method. In order to build on the gains in efficiency that continuous casting can offer, much work is currently being done to remove certain key parts of the process as it stands, and to reduce the thickness of the strand that it produces. Unnecessary reheating stages may therefore be avoided, and the number of rolling operations required to finish the product may be reduced. The resulting processes (hot charging, direct rolling, thin slab casting and strip casting) offer very significant gains over conventional continuous casting in a number of important areas, and are therefore very attractive to steel producers. However, the elimination of parts of the continuous casting process poses a serious problem when many grades of steel are being cast because it means that one must ideally be able to guarantee the quality of the strand produced by the caster. At present this is not possible, particularly in microalloyed grades, because these and other classes of steel are prone to forming cracks on the surface of the as-cast strand.

The cracks that we are concerned with here form on the top surface and edges of the as-cast product, transverse to the casting direction, and appear as the strand, which is

cast in a curved mould, is straightened. This straightening operation takes place when the surface of the steel is in the vicinity of the austenite-plus-ferrite two-phase region and therefore the formation of transverse cracks is, in many cases, strongly linked to the austenite-to-ferrite phase transformation.

Deformation, as is applied during the straightening operation, is known to have a significant effect on diffusional transformations; but the effect of strain, strain rate, test temperature and prior austenite grain size on the austenite-to-ferrite phase transformation, and the resulting effect on the ductility of the steel in question, has not yet been fully determined. This is the basis of the present investigation. The general objective of this project is to use previous and some of the present work to examine the effect of the aforementioned parameters (determined in compression) on the austenite-to-ferrite phase transformation. These findings will then be related to the tensile hot ductility of the same steel under similar conditions—the hot ductility of a steel being taken as the measure of its susceptibility to transverse cracking.

In Chapter 2, a review of relevant literature is presented; this review is split into four major sections. In the first section, the continuous casting process is introduced and possible improvements to this casting route are presented. This is followed by a brief review of potential quality problems in this process and the various measures that are currently taken to combat them. In the second section, the hot ductility of steel in the pertinent temperature range is described; various methods of determining this property are presented, and factors that affect its value are discussed. The third section contains a description of the austenite-to-ferrite transformation under static conditions and the effect that various parameters can have on this phenomenon. Finally, the closing section of Chapter 2 is devoted to a discussion of the deformation of steel in the intercritical region, and the effect of such deformation, as suggested by other authors, on the austenite-to-ferrite phase transformation.

In Chapter 3, the experimental methods, materials and apparatus used in this work are described. Schematic diagrams of the compression and tensile tooling arrangements are given, the principles behind the testing control programs are explained, and the thermal

cycles employed in this work are plotted. Optical and scanning electron microscopy were used to examine specimens after testing, and the procedures used therein are also described in this chapter.

The experimental results are described in Chapters 4 and 5. Chapter 4 contains static and compressive test data, including flow curves and micrographs, that attempt to document the effect of compressive deformation on the austenite-to-ferrite phase transformation. Chapter 5 presents the tensile results: flow curves, optical and scanning electron micrographs, and quantitative metallography data are displayed along alongside tensile hot ductility results.

The above results are discussed in Chapter 6, beginning with the apparent effect of strain, strain rate, test temperature and prior austenite grain size on the austenite-to-ferrite phase transformation, as determined in previous closely related work. The impact this effect might have on the industrial problem of transverse cracking during continuous casting is then discussed in the final section of this chapter.

Finally, the conclusions reached in the discussion are presented in concise form in Chapter 7.

Chapter 2

Literature Review

2.1 Industrial Perspective—Continuous Casting

2.1.1 Origins of the Continuous Casting Process

> "Among the numerous inventions that are from time to time brought under public notice, a certain proportion are from some cause or other allowed to fall out of sight and be forgotten... Some inventions, which appear well worthy of a trial, are never put to a practical test through having appeared at a time when the state of the particular manufacture to which they apply was not so far advanced as to render the proposal feasible with the then existing state of knowledge..."
>
> Sir Henry Bessemer, FRS, 1891.[1]

For the majority of the past 200 years, the large-scale conversion of liquid steel into usable solid form has been achieved by the use of a batch process known as ingot casting. In this process, which is shown schematically in Fig. 2.1, molten steel is first cast into ingot moulds, which are allowed to solidify. The ingots are then removed from the moulds and reheated in a soaking furnace to around 1,300°C, in order to prepare them for rolling in either the blooming or slabbing mill, where the aspect ratio of the final product is

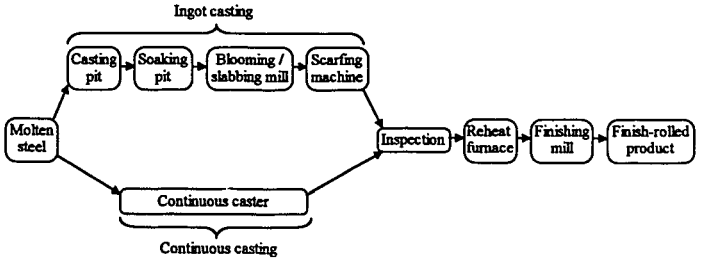

Fig. 2.1 Comparison of the ingot and continuous casting process routes.

decided. The resulting semi-finished products are cooled, scarfed (i.e. part of their surface is removed by grinding), and inspected. Finally the blooms or slabs are reheated for hot rolling.

As early as 1840, the idea of solidifying steel by some more continuous method than ingot casting had come to light. Sellars (1840), followed by Laing (1843) and Bessemer (1846) conducted experiments based on this idea. However, technical problems associated with the high temperature and low thermal conductivity of molten steel led to the failure of these efforts, although some techniques were successfully applied to the casting of non-ferrous metals with low melting points.

In 1889, after some years of apparent inactivity in the development of continuous casting technology for steel production, Daelen obtained a patent[2] in which he described a process that incorporated many of the essential features of modern continuous casting machines. In that process, a continuous stream of molten steel was to be poured into a mould that was open at both ends; upon leaving the bottom of the mould, the solidified strand would be passed to a secondary cooling system and be withdrawn by pinch rollers. However, it was evident that problems still existed, particularly in the region of the mould, where the newly solidified strand would stick to the walls, halting the process and resulting in a potentially very dangerous situation. This problem was not solved until 1938, when Junghans[3] obtained a patent for a mould oscillation system wherein the mould was made to reciprocate in a vertical plane, giving it almost continuous motion relative to the strand and therefore preventing sticking.

It was not until after the Second World War that pilot-scale plants using this technology began to emerge, and not until the early 1960s that the popularity of the process began to grow significantly. With its major problems solved, continuous casting was a very attractive casting route because it offered significant gains both in efficiency, and in as-cast product quality.

The use of continuous casting saves money in a number of ways. Firstly, it reduces energy consumption through removing as many as four of the five operations that are needed in ingot casting (Fig. 2.1). Perhaps more importantly, continuous casting avoids the need for at least one of the reheating processes; this decrease in energy usage has the added benefit of lessening pollution. Reducing the number of processes also moderates manpower requirements, and the automatic nature of many of the processes that are left takes this even further. Higher product quality results in improved yield, which both increases productivity and gives a further energy saving because less material must be scrapped and subsequently recycled. The speed of the continuous casting process means that less stock must be held, and delivery times can be shortened. As a summary of the above, the major advantages of this process over the ingot process, and the reasons for these advantages, are listed below:

1. *Reduced energy consumption*—at least one heating process removed;
2. *Improved yield*—less scarfing required due to improved surface quality;
3. *Lower manpower requirement*—more automatic handling and fewer steps;
4. *Reduced capital costs for new plants*—less equipment, lest inventory, therefore less space required.

These benefits have made the continuous casting process by far the most important casting route in modern steelmaking. Fig. 2.2 shows how its use has increased over the past 30 years: in 1991, 83% of the Western World's crude steel production was cast continuously; in the EEC, the figure was 90%.[4]

2.1.2 The Modern Continuous Casting Process

In the modern continuous casting process (Fig. 2.3), molten steel is introduced to the mould via a tundish, which acts to distribute molten steel into either one strand, or over a number of strands that are being simultaneously cast. It also acts as a reservoir during ladle changing. The tundish helps to remove inclusions from the steel by the action of various weirs and dams that stop these impurities from passing into the mould.

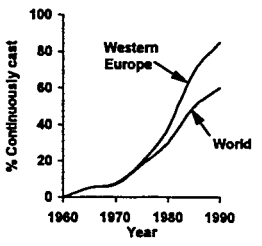

Fig. 2.2 Proportion of crude steel produced by continuous casting.[5]

Having entered the mould, which it does through a refractory 'submerged entry' nozzle so as to avoid reoxidation, the steel begins to solidify, starting at the mould wall. The mould is the primary cooling zone and is generally made of a copper alloy and cooled by large quantities of water. As was mentioned in the previous section, the mould is made to oscillate relative to the strand in a vertical plane in order to prevent sticking. The reciprocation of the mould is often sinusoidal and always incorporates what is known as 'negative strip', i.e. the velocity of the mould exceeds that of the strand on the downward

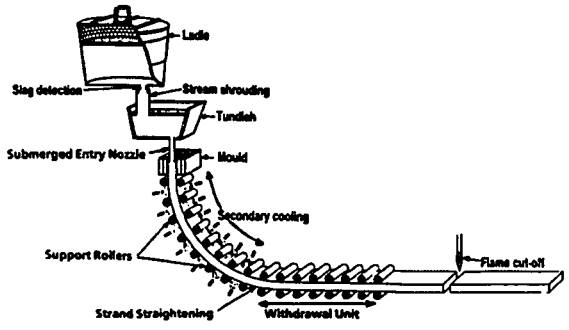

Fig. 2.3 Schematic diagram of a modern slab casting machine.[6]

stroke. Negative strip is vital in preventing 'breakouts'—where the skin of the solidifying strand breaks and releases the molten metal held inside. A breakout can often result in the destruction of significant parts of a continuous casting machine, and can therefore be extremely expensive. It should be noted that mould oscillation, while being vital to the successful operation of the machine, is also associated with the formation of transverse ripples (oscillation marks) on the surface of the steel. Oscillation marks are closely linked to the problem of transverse cracking that is introduced in section 2.1.4, and is the industrial root of this study.

In modern continuous casting machines moulds are invariably curved, although this is not the only possible configuration.[7] The curvature permits casting to be performed vertically under gravity, and extraction of the solidified strand to be performed horizontally, allowing for a truly continuous process. However, one major implication of a curved mould is that at some point the strand must be straightened.

As the strand emerges from the mould it enters the secondary cooling zone where it is cooled using water sprays. At this stage the steel is carefully supported using guide rollers so as to minimize the chance of breakout. The strand leaves the secondary cooling zone as the tangent to its curve tends towards the horizontal, whereupon it is straightened (or 'unbent') using an array of rollers in what is known as the 'unbending' operation. The resulting horizontal product is withdrawn using driven rollers and cut into appropriately-sized lengths by a flame cutter that is driven forward (away from the machine) at the same rate as the exiting strand, thus giving an edge perpendicular to the casting direction.

2.1.3 The Future of Continuous Casting

The present trend in continuous casting is to remove parts of the process that can be made unnecessary, notably the inspection stage. If product quality can be either guaranteed, predicted throughout production runs, or measured without cooling the strand, then the need for room temperature inspection disappears, as does the need for a significant part of the subsequent reheating process. The removal of the inspection stage in conventional continuous casting gives rise to two possibilities in improving the process, these are termed *hot charging*, and *direct rolling* (Fig. 2.4).

In the practice of hot charging, the continuously cast strand is taken off the continuous caster and put into the reheat furnace *without* first cooling it to room temperature. This leads to a saving both in the energy needed for reheating, and in the time and space that would otherwise be occupied for cooling and inspecting the slabs as they come off the caster. This practice is becoming commonplace in easier-to-cast grades of steel.

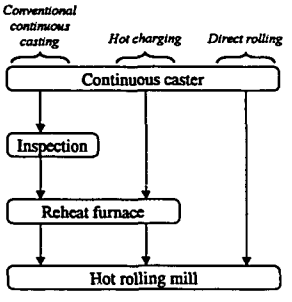

Fig. 2.4 Stages that could be removed from the continuous casting process.

In the practice of direct rolling, the strand is taken off the caster and put directly into the hot rolling mill, often via a continuous soaking furnace. This eliminates the reheating stage almost altogether. The widespread adoption of direct rolling in the future, however, requires a significant increase in casting speed since the throughput of a modern caster is much lower than that of a modern hot rolling mill. This increase in speed is likely to be achieved by casting thinner sections as raising casting speed while maintaining current product dimensions would mean building long and expensive casters. Even though casting thinner sections introduces a myriad of new problems, it is widely seen as being the next step in the development of the continuous casting process.

Aside from the partial removal of one heating stage, bringing as-cast dimensions closer to those of the final product has many other potential advantages, mainly related to the removal of parts of the subsequent rolling processes. The number of operations that can be removed depends on how close the as-cast strand is to its intended final size; the attempts that are at present being made to reduce as-cast dimensions can largely be distinguished by the extent to which they might achieve this (Fig. 2.5).

Thin slab casting is intended to produce slabs ranging from 20-80 mm thick (conventional slab thickness is typically around 200 mm). Slabs of these dimensions do not require roughing and so may be passed directly to the hot finishing mill. Some plants

based around thin slab casters are currently in operation, perhaps the most notable being Nucor's Crawfordsville plant[8] in Indiana, USA, which was the first plant of this kind to be built on a greenfield site. Two more radical processes, *strip casting* and *thin strip casting*, are still in the developmental stage.[9] Strip casting has the potential of eliminating the hot strip mill altogether, allowing the product either to be sold immediately after casting, or passed directly to the cold rolling mill, depending on its intended use. Thin strip casting may be able to eliminate all processing bar the casting itself even for 'cold rolled' strip, provided that the desired mechanical properties can be obtained in this manner. It should be noted that this final proviso, of course, applies equally to all the new techniques mentioned here.

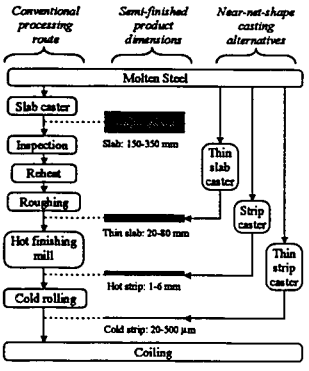

Fig. 2.5 Near-net-shape casting possibilities for flat rolled products.[10]

2.1.4 Quality in Continuous Casting

As was mentioned in the previous section, in order for either hot charging or direct rolling to be applied to the casting of a given steel, it must be possible either (a) to guarantee a certain level of quality in the as-cast product throughout a production run; (b) to use parameters measured during the casting of a given slab (e.g. mould and cooling water temperatures, tundish level control, and withdrawal force) to perform real-time prediction of whether defects are likely to be found in that slab;[11] or (c) to measure surface quality after casting without cooling the strand. The latter possibility is at present the most widely used and is termed 'on-line hot surface inspection'. Apparatus designed for this purpose must be capable of detecting, marking, and categorising flaws on the surface of the steel at temperatures greater than 900°C and roller table speeds of up to 1.5 m s^{-1}. Considerable research effort has been expended in this area[12] and has produced devices

based on optical, thermal, electromagnetic, and ultrasonic processes; the most widely used of these is the optical variety.[13]

As in any quality control system though, the most desirable solution is the first: to be able to guarantee product quality. The focus of this study is to further understanding of one mechanism by which certain imperfections are thought to form, and thereby to contribute to our ability to guarantee the quality of continuously cast semi-finished products.

A number of categories of defect can be found in continuously cast products; Brimacombe and Sorimachi[14] identified 11 different types of imperfection, examples of which are inclusions, blowholes, internal segregation, and cracks. However, since inclusions and blowholes can now be confidently controlled using well known steelmaking and casting procedures,[15] and the effects of segregation are reduced by the hot rolling process, cracks, particularly surface cracks, are presently the biggest single issue in improving the quality of continuously cast products. The International Iron and Steel Institute (IISI) categorised 8 types of surface defect[16] that can be found in this type of product; however, in this survey, we are specifically concerned with the transverse facial and edge variety of surface cracks. These are distinct from other types of surface imperfection, as detailed by the above authors, because they are thought to develop *outside* the mould during the unbending operation when the solidification process, at least at the surface, is complete.[14]

In order for cracks to form at a given location on the surface of the strand, two conditions must be satisfied:[17]

1. a stress system must be in operation, and it must be tensile in nature;
2. the fracture strength at that point on the surface must be exceeded.

There are a number of sources of stress on the strand during the continuous casting process (two of which were mentioned earlier), the analysis of which has become very advanced with the application of finite element methods. The explanation of these studies is beyond the scope of this thesis, however, Lankford[18] has produced a good qualitative

summary of the sources of stresses acting on a continuously cast strand in which he suggested that these stresses may be separated into essentially 4 major areas:

1. *mould friction forces*—related to friction between the newly solidified strand and the reciprocating mould;
2. *thermal stresses*—due to thermal gradients both through the solidifying skin and along the axis of the casting;
3. *ferrostatic pressure*—exerted on the skin by the molten core of the strand—important both in and below the mould;
4. *bending forces*—imposed during the bending or 'unbending' of the strand in order to withdraw the product horizontally.

2.1.5 Transverse Cracks

Transverse cracks are generally fine and can penetrate to a depth of 5-8 mm below the surface of the strand. The cracks can be difficult to detect on the as-cast surface and so scarfing of difficult grades after casting in order to reveal them is commonplace. There is still no consensus about the origin of transverse cracks (i.e. the point at which they first appear). Cracks generally form at the roots of oscillation marks and have been found to contain mould powder: they are therefore generally thought to be initiated in the mould.[19] However, cracks have also been observed to nucleate during bend tests performed at around 800°C,[20] which suggests that nucleation in the mould is not a necessary condition for transverse crack formation. Mintz et al.[21] suggested that oscillation marks act as notches, creating stress concentrations at their roots. This hypothesis is supported by Maehara et al.[22] who found that increasing the depth of notches in tensile specimens generally reduces elongation in the temperature range 800-1,100°C; notch radius was found to be unimportant, as sharper notches became rounded in the early stages of deformation.

Crack propagation takes place during the unbending operation, where the major source of stress is that induced by the strain imposed to achieve the desired shape change. It is evident (Fig. 2.6.) that in order for the strand to accommodate the imposed change in

its geometry, its top surface must be placed in tension and its bottom surface in compression. However, the strain distributions across the width of the strand and through its thickness depend on whether the strand is completely solidified, or if it still contains a liquid core (as is often the case in modern, high speed machines).

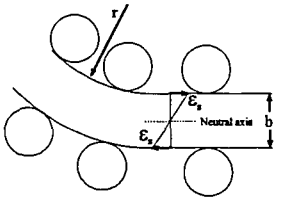

Fig. 2.6 *Through-thickness strain distribution in a fully-solidified strand during single point straightening.*[6]

With the strand completely solidified, simple beam bending theory, as suggested by Lankford,[18] gives a reasonable approximation of the strains (ε_s) imposed at the surfaces:

$$\varepsilon_s = \frac{b}{2r} \qquad \textit{Eq. 2.1}$$

where b is the slab thickness (typically 200 mm) and r is the radius of curvature of the strand (between 8 and 10 m).

In the case of straightening with a liquid core, the middle portions of the upper and lower parts of the solidified shell are considered as separate beams, while the influence of the skin formed at the edges of the strand is measured by considering its thickness relative to the total width of the section. This leads to two different models for deformation of a strand with a liquid core: the '*soft-*' and '*hard box*' models, as illustrated in Fig. 2.7.

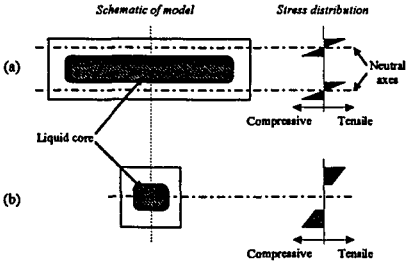

Fig. 2.7 *Strain distribution in solidified shell using (a) the 'soft box' approach, and (b) the 'hard box' approach.*[6]

The soft box approach assumes the strand to be a 'soft' box, with the upper and lower skins acting entirely independently. This is most likely to be applicable in products such as slabs, where the aspect ratio

is high, and where the shell thickness is small when compared to the slab width. In this case, the surface strains and solid/liquid interface strains are given by

$$\varepsilon_s = \varepsilon_i = \frac{t}{2r} \qquad \textit{Eq. 2.2}$$

where ε_s = outer surface strains;

ε_i = solid/liquid interface strains;

t = shell thickness;

r = machine radius.

In the hard box case, bending is assumed to be strongly influenced by the deformation of the solidified edges and therefore the surface strains are given by Eq. 2.1, i.e. the same equation as for the completely solidified case. The solid/liquid interface strains in the hard box model are given by

$$\varepsilon_i = \frac{b-2t}{2r} \qquad \textit{Eq. 2.3}$$

It has been demonstrated, using finite element techniques, that the soft box approach is appropriate for slabs or large blooms, and that the hard box model is only valid for billets and small bloom sections.[23]

It can be seen from Eq. 2.1, Eq. 2.2, and Eq. 2.3 that, assuming that large strains are bad for quality, the 'worst case' scenario, for the purposes of preventing cracks that nucleate on the surface of the strand, is that expressed by either the hard box or solid models as these models give the highest strains for given values of b and r. If a realistic range of values for these two parameters is substituted into Eq. 2.1 (e.g. $150 < b < 350$ mm and $8 < r < 10$ m), then the slab surface strain is found to vary between 0.8 and 2.2%.

The strain rate under continuous casting conditions can be estimated by:

$$\dot{\varepsilon} = \varepsilon \frac{v}{l} \qquad \textit{Eq. 2.4}$$

where v is the casting speed (typically in the range 0.8 to 1.8 m min^{-1}) and l is the distance over which the bending stress develops, a distance that can vary considerably depending on machine design. In order to keep strain rates low, some machines are designed with

multi-point bending, where the strand is bent slightly at a number of different stages through the machine. Using Eq. 2.4, Lankford estimated the strain rate during unbending in continuous casting to be between 5×10^{-4} s^{-1} and 7×10^{-3} s^{-1}.[18]

2.2 The Hot Ductility of Steel between 700 and 1,000°C

The formation of transverse cracks during the continuous casting of steel has been firmly linked to the existence of a temperature range in which steels exhibit low ductility. The straightening operation is carried out while the surface of the strand is between 700 and 1,000°C, over which range steels tested in uniaxial tension will fracture after a relatively small elongation.

2.2.1 Measurement of Hot Ductility

The test that best simulates the mechanical aspects of unbending is the hot bend test.[18] In this procedure, 'hot ductility' is determined by assessing the severity of surface cracking produced during the experiment; this evaluation can be difficult to perform and so the test has rarely been used. Alternatives to this method, which attempt to mimic the mechanical situation found in beam bending, have been developed—one a variation on the hot compression test,[24] another a method of solidifying notched tensile specimens in situ.[25] However, because of the easy availability of standard equipment and the comparatively simple procedures associated with it, the laboratory technique that has been used in the vast majority of the hot ductility work carried out to date is the isothermal, uniaxial hot tensile test.

During a hot tensile test, a specimen is commonly heated to some temperature above the solution temperature of any microalloy precipitates, both to dissolve these particles, and to attain a coarse grain size similar to that found in the continuously cast strand. The sample is then cooled to test temperature, in this case normally between 700 and 1,000°C, and deformed isothermally to fracture, often using a servo-hydraulic load frame. Upon fracture, one of the resulting specimen halves may be quenched in order to preserve the microstructure that existed at failure. The 'hot ductility' is then taken to be either the reduction in area, or the total elongation, at fracture; both are normally

expressed as a percentage. The more usual quantity to use is the reduction in area (%RA) because it is easy to measure and is not dependent on specimen geometry.

However, it should be noted that, even if one ignores the mechanics of the applied stresses, the hot tensile test does not, in any of its guises, closely simulate the straightening operation in continuous casting. The conditions imposed during these tests differ in several important ways from the real situation, the major differences being the thermal history of the sample (and therefore the microstructure), and the amount of straining imposed.

In the case of the straightening operation, the microstructure near the surface of the strand is columnar and very coarse, with grains up to 10 mm in length; the material here is highly segregated and the surface is significantly oxidised. In most hot tensile work, on the other hand, the grain size obtained is smaller, of the order of 300 μm, and the microstructure is equiaxed. Also, in the laboratory, much effort is often expended in homogenising the material and protecting the specimen's surface from oxidation. During unbending, the surface of the strand undergoes significant cyclic temperature variations (see section 2.2.3.3), whereas in isothermal tensile testing the temperature, of course, remains constant. Finally, in the case of continuous casting, the strain imposed on the top surface of the strand during unbending, as has already been mentioned, is between ~1 and 2%, whereas in the case of tensile testing to failure, the elongation in the trough may be as much as 50% and is normally non-uniform.

In its defence, the hot tensile test does seem to redeem itself when used intelligently in examining specific problems. Mintz and Abushosha[26] found that the test is very sensitive to the heat treatment employed (see section 2.2.3.2). For instance, it was found that for examining the influence of S and Ti (i.e. elements that do not otherwise go completely back into solution), the procedure of casting tensile specimens and cooling them directly to test temperature is likely to be the best method of simulating the actual unbending process. On the other hand, the solution treatment route, as outlined above, was found to be an excellent method for examining the effect of Al, Nb and V on ductility.

The hot *compression* test has also been used in work related to hot ductility,[27] and it has been used in a significant part of this study. Compression testing has the advantage that it avoids the problem of necking and so, in theory, relatively homogeneous and precise strains can be applied. Further, specimens deformed in compression can be quenched at any point during deformation, whereas in tension, one very often has to wait for failure to occur before quenching is possible. However, it should be noted that, with the possible exception of the amount of strain applied, the same discrepancies exist between the conditions imposed during the hot compression test and those that prevail during the unbending operation as were described above for the tensile case.

2.2.2 Hot Ductility Curve Between 700 and 1,000°C

If a number of isothermal hot tensile tests are performed on a given steel over the 700 to 1,000°C temperature range, and the resulting %RA values are plotted against test temperature, a curve resembling that in Fig. 2.8 is commonly obtained. It can be seen that there is a significant drop in ductility (%RA) between ~700 and 900°C, what might be referred to as a 'ductility trough'. In order to explain the reasons for its existence, it is useful to split this trough into three sections, as shown in the figure:

1. the trough or region of embrittlement;
2. a high ductility, high temperature (HDH) region;
3. a high ductility, low temperature (HDL) region.

Each of these regions is discussed individually below.

2.2.2.1 Region of Embrittlement

Fracture in the region of embrittlement at the low strain rates that apply in continuous casting is invariably by intergranular failure.[21] The fracture surfaces are either smooth, or are covered in fine dimples (the relics of microvoids), suggesting two distinct fracture mechanisms.

Smooth fracture surfaces are caused by grain boundary sliding in the single phase austenite region. Grain boundary sliding may be thought of as plastic deformation that is

closely confined to the vicinity of the grain boundaries. This occurs in austenite rather than in ferrite because, as is explained in section 2.4.1, recovery is favoured in the latter, giving rise to low flow stresses in the bulk of the material. Cracking occurs by tearing at triple points (Fig. 2.9), where large stresses build up that are not accommodated by the lattice.

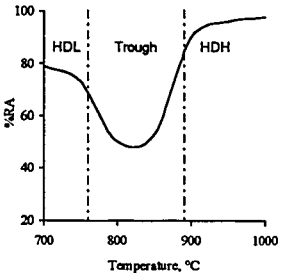

Fig. 2.8 Typical variation of %RA values over the range 700 to 1,000°C.[21]

Grain boundary sliding is essentially a creep fracture mechanism and is therefore typically associated with strain rates below 10^{-4} s^{-1} (i.e., lower than those found in most continuous casters). However, fracture has been observed to occur by this mechanism at strain rates of the order of 10^{-3} s^{-1}, and Ouchi and Matsumoto[28] have observed grain boundary sliding in Nb containing steel at rates as high as 10^{-1} s^{-1}.

Dimpled fracture surfaces are linked to preferential deformation around the austenite grain boundaries, causing the formation of microvoids; these link up and eventually cause failure. This preferential deformation can be caused by two separate mechanisms:

1. precipitate free zones;
2. thin ferrite films.

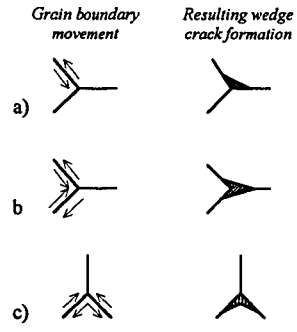

Fig. 2.9 Schematic models of wedge crack formation by grain boundary sliding.[29]

In microalloyed steels that have been solution treated before being cooled to the test temperature, Mintz et al.[30] found that microalloy precipitation takes place during deformation in the austenite. The formation of relatively coarse precipitates at the grain boundaries is accompanied

by the formation of a precipitate free zone (PFZ) around the grain boundary; this is accompanied fine matrix precipitation in the remainder of the material, which leads to considerable strengthening. The PFZ therefore lacks strength relative to the rest of the matrix, and so deformation is concentrated in this area; voids form at grain boundary precipitates and failure results.[31]

At temperatures high in the γ-plus-α two-phase region, thin films (~5-20 μm thick)[21] of ferrite form at austenite grain boundaries. At a given temperature, ferrite has a lower flow stress than austenite—ferrite work hardens less readily since dynamic recovery is more difficult in austenite[32] (see section 2.4.1). When these two phases are both present, therefore, in a material that is being plastically deformed, a larger proportion of the strain will be concentrated in the ferrite. This leads to ductile void formation at stress concentrators such as MnS inclusions, and eventual void linking and failure (Fig. 2.10).

Crowther and Mintz,[33] amongst others, have shown that the formation of these ferrite films is induced by deformation. Under static, isothermal conditions, ferrite would first be expected to appear at the Ae_3 temperature, that is the equilibrium transformation temperature for the steel in question (see section 2.2.3). Under more realistic (continuous cooling) conditions, ferrite would first be expected to appear at the Ar_3 temperature, referred to as the continuous cooling transformation temperature. This varies with cooling rate but must, of course, always be lower than the Ae_3. However, under dynamic (i.e. straining) conditions, ferrite has been shown to appear at temperatures well above the static Ar_3, and even up to the Ae_3 (see section 2.4.2.3). Mintz et al.[34] have shown that even the small strains associated with the unbending operation are sufficient to induce ferrite formation above the static Ar_3 in 0.1%C steel.

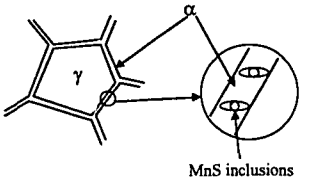

Fig. 2.10 Schematic diagram showing mechanism of transformation-induced intergranular failure.[21]

2.2.2.2 High Ductility High Temperature Region

Ductility rises sharply towards the higher temperatures shown in Fig. 2.8. When the Ae_3 temperature is approached, the ferrite volume fraction tends towards zero, thereby inhibiting strain concentration in this softer phase. This mechanism is, of course, only effective in improving ductility up to the Ae_3; once the single-phase austenite region is entered, other mechanisms are responsible for the material's behaviour.

At these higher temperatures, the driving force for precipitation is reduced, meaning that fewer precipitates will be found in the matrix and at grain boundaries, and therefore less strain concentration by the action of precipitate free zones should be encountered. Also, Grant and co-workers[35] have shown that crack formation by grain boundary sliding in creeping alloys occurs most easily in the presence of grain boundary particles; a reduction in the number and size of grain boundary precipitates should therefore have an effect on this mechanism. However, grain boundary sliding can occur more readily as the temperature increases, so that it is possible for ductility to actually deteriorate.

In more than one study,[36, 37] the lower temperature limit of the HDH region has been found to coincide with the occurrence of dynamic recrystallization, which is thought to improve the ductility of steels because it occurs by the movement of grain boundaries. Grain boundary migration isolates grain boundary cracks, effectively moving them closer to the centres of grains where it is more difficult for them to grow and subsequently coalesce. However, Mintz et al.[38] suggest that this correlation exists because, at temperatures below the Ae_3, dynamic recrystallization is stifled by the presence of thin bands of ferrite around austenite grains, which, of course, are not good for the ductility. The above authors postulate that if the temperature were high enough to remove all ferrite (i.e. $>Ae_3$), but too low for dynamic recrystallization, the ductility would still be low because at this point grain boundary sliding is a significant embrittling mechanism. Whether the ductility would improve at this point, depends on the relative effects of the two mechanisms. Such knowledge is of course very important to the continuous casting situation.

As the temperature is further increased in the single-phase austenite region, the rate of grain boundary sliding is increased, but this occurs as the critical strain for dynamic recrystallization decreases, in many cases resulting in a net improvement in ductility. It should be noted that migrating grain boundaries can be pinned by precipitates, and therefore dynamic recrystallization can be inhibited. The removal of precipitates by raising the test temperature, as well as limiting grain boundary sliding and preventing strain concentration, can thus also effect the ductility in this third manner.

Finally, increasing the test temperatures leads to a reduction in flow stress in the bulk material. This increases compliance in the matrix with strains occurring at grain boundaries and thus decreases strain concentration in these areas, thereby increasing the material's ductility.

2.2.2.3 High Ductility Low Temperature Region

The increase in %RA values at the lower end of the ductility trough is largely due to the presence of significant quantities of ferrite in the material: ductility reaches a maximum in this region when there is around 50% ferrite present prior to deformation.[21] Ferrite is far more ductile than austenite and is only detrimental to ductility when present as thin films—a result of all the strain being concentrated in this phase. The strength differential between austenite and ferrite decreases with temperature,[32] and this coupled with the rapidly increasing amount of ferrite available to accommodate the strain results in a significant increase in ductility when the temperature is further reduced.

2.2.3 The Effect of Test Variables on Hot Ductility

2.2.3.1 The Effect of Strain Rate

Increasing the strain rate in a hot tensile test, over the range of strain rates found in the unbending operation, invariably improves the hot ductility, and can eradicate the trough entirely.[39] Fig. 2.11 shows the results of one study in which raising the strain rate by several orders of magnitude resulted in a narrowing of the ductility trough, a reduction in its depth, and the displacement of the trough's upper bound to lower temperatures. This displacement is normally present and is due to the reduction in the amount of time

available for certain critical processes to occur. These process include dynamic precipitation, diffusion-assisted void nucleation and growth, and dynamic recovery in ferrite. The latter process, it has been suggested,[27] results in the work hardening of any thin films of ferrite formed at the austenite grain boundaries, encouraging the strain to be taken up by the γ, thus leading to an increased amount of deformation induced ferrite and better ductility. Increasing the strain rate has also been observed to cause a decrease in the proportion of the fracture strain attributable to grain boundary sliding.[28]

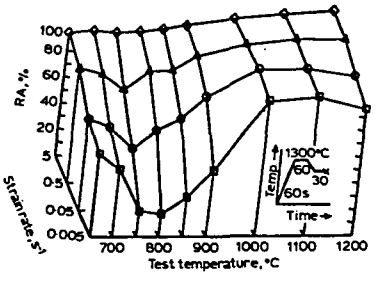

Fig. 2.11 Dependence of ductility on strain rate and test temperature for Nb-bearing steel.[39]

When unstable fine precipitates (e.g. FeMn sulphides) are present, *decreasing* the strain rate has also been shown to improve ductility;[40] in this case, precipitate coarsening seems to be the beneficial mechanism. Niobium-containing steels have been shown to benefit from a similar phenomenon (coarsening of Nb(C, N) precipitates) at very low strain rates (10^{-4} to 10^{-6} s^{-1}).[41]

2.2.3.2 Effect of Reheat Temperature

As was mentioned in section 2.2.1, the results gained from a hot tensile test are very sensitive to the thermal cycle imposed. This sensitivity is, of course, due to the effect that the thermal cycle has on the microstructure of the specimen.

In most cases, specimens are heated to some austenitizing temperature (usually between 1,100 and 1,300°C), cooled to test temperature, and then tested isothermally to failure. This treatment gives a relatively coarse grain size, redissolves most precipitates, and aids the examination of the effects of Al and Nb; compared with the directly cast method, more Nb is available for precipitation in fine form during deformation. However, this form of heat treatment does not allow full investigation of the effects of elements such

as Ti and S, since these in their combined forms as TiN and MnS do not fully dissolve until higher temperatures.[26]

Casting samples in a Gleeble machine (i.e. reheating them to some point above the liquidus temperature) is thought to be the best method of *simulating* the thermal conditions that lead up to the unbending operation.[26] This is the only procedure capable of assessing the effect of elements that form high-melting-point precipitates such as those mentioned above. However, this type of treatment tends to suppress changes in ductility that result from other compositional variations because precipitation is often coarse in the as-cast state.

In samples heated directly to test temperature, grain sizes are relatively fine and thin films of ferrite do not form. It is generally accepted that the ductility trough in such experiments results from grain boundary sliding, encouraged by the presence of any fine precipitates. In this case, the low temperature limit of the ductility trough is tied to the end of the ferrite-to-austenite transformation on heating and extends to a temperature high enough to dissolve and/or coarsen the precipitates so that they can no longer effectively pin grain boundaries, or cause cavity linkage due to their close proximity.[42]

2.2.3.3 Effect of Thermal Cycling

The surface temperature of the slab varies dramatically as it passes through the continuous caster. As it moves away from the bottom of the mould, the surface comes into contact both with cooling water sprays, and with guide rollers, which are water cooled. This leads to considerable temperature cycling, as evidenced by Fig. 2.12. It can be seen from this figure that the strand surface temperature drops considerably (in this case around 100°C) during contact with each of the rollers, then rises rapidly, only to fall slightly again as a result of the cooling sprays. The reason for the sudden rise in temperature, of course, is the fact that the core of the slab is much hotter than the surface.

Simulations involving cyclic heat treatments have been performed.[43, 44] These have shown that in C-Mn-Al and C-Mn-Nb-Al steels, allowing the temperature to drop below the test temperature during the prior heat treatment causes an increased amount of fine precipitation, and thereby reduces ductility. Where the temperature drops low enough for some ferrite to form, it would be expected that precipitation would be further enhanced, and therefore the ductility reduced further.

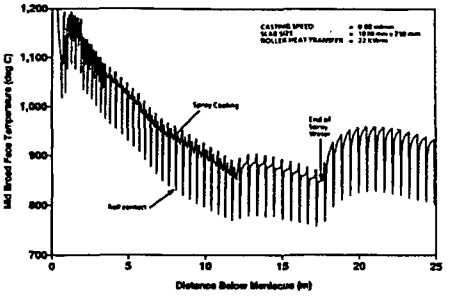

Fig. 2.12 Surface temperature profile down the mid broad face for a 1,830 mm × 230 mm slab.[6]

2.3 The Austenite-to-Ferrite Phase Transformation Under Static Conditions

Upon cooling slowly to the A_3 temperature,[45] γ-iron (face-centred cubic) begins to transform into α-iron (body-centred cubic). This transformation occurs at 910°C in pure iron, but is progressively moved to lower temperatures as the carbon content is increased (assuming no other alloying elements are added), down to a minimum of 723°C, the eutectoid temperature.

The growth of ferrite in an austenite matrix is a diffusion-controlled process;[46] that is, the rate at which it occurs is determined by the rate of diffusion of some species (in this case carbon) through the material. The maximum solubility of carbon in γ-iron is 2.11 wt% and occurs at 1147°C, whereas the maximum solubility of C in α-iron is 0.02 wt% at 723°C. This two-order-of-magnitude disparity in C solubility in the respective lattices is due to differences in the size of interstitial positions; even though austenite is in the close-packed configuration,[47] its interstitial sites are larger than those found in ferrite, and it is

therefore able to accommodate larger amounts of carbon. The result is that when γ decomposes into α, carbon must diffuse across the boundary between the two phases and away through the γ lattice.

If the transformation is allowed to approach completion, the solubility limit of C in the austenite will eventually be reached and cementite (Fe_3C) will be formed. This is a metastable phase, in that it will remain indefinitely at room temperature, but if heated to between 650 and 700°C for several years it will slowly transform to α-iron and graphite, the stable form of carbon. Given the sloth of this transformation, cementite is, for practical purposes, considered stable.

2.3.1 The Effect of Cooling Rate

The γ-to-α transformation may be detected experimentally during heating or cooling using either thermal analysis or dilatometry. However, as was mentioned in section 2.2.2.1, some hysteresis is observed in the phase change, and as a consequence three values for the A_3 temperature can be obtained: Ac_3 for heating (chauffage), Ae_3 (equilibrium), and Ar_3 for cooling (refroidissement). The values obtained for Ac_3 and Ar_3, relative to Ae_3 for a given steel, are affected by the rates of heating or cooling used in their measurement, which can also affect the morphology of the ferrite formed (see section 2.3.4). These values are also influenced by the austenite grain size (see section 2.3.2): refining the austenite structure would lead to more ferrite nucleation sites and consequently a higher Ar_3 temperature for a given cooling rate and composition.

2.3.2 Effect of Alloying Elements on the Ae_3 Temperature

The addition of alloying elements to a steel can dramatically affect the γ-to-α transformation. Elements such as Ni, Mn, Co, Cu, C and N are austenite formers; that is, they lower the Ar_3 and retard the decomposition of γ. Elements such as Si, Al, P, Cr, V, Mo, W, Ti, Ta, Nb, and Zr, on the other hand, are ferrite formers; they raise the Ar_3 but retard γ decomposition by slowing the diffusion of C in the austenite matrix and by other mechanisms such as grain boundary enrichment. All of the aforementioned ferrite formers

except Si, Al and P are also strong carbide formers and will therefore precipitate alloy carbides independently, further complicating their effects on the phase transformation.

2.3.3 Ferrite Nucleation and Growth

The nucleation of ferrite in the austenite matrix is, of course, a heterogeneous process. Suitable sites are discontinuities such as free surfaces, stacking faults, dislocations, and particularly grain boundaries, all of which increase the free energy of the material.[48] The formation of ferrite nuclei at these crystalline defects, and the resulting complete or partial destruction of the imperfection, is a thermodynamically favourable event: the activation energy for ferrite precipitation is effectively reduced or eliminated altogether by the free energy released as the discontinuity is removed. The proportion of ferrite nuclei that result from each of these types of defect depends upon the free energy available in each case, and the number of a given type of defect present in the matrix. As was shown by Clemm and Fisher,[49] the most favourable sites are grain corners, edges, and surfaces, respectively; however it should be noted that the density of sites available in each case decreases in the same order. In a fine-grained specimen, where there are a large number of grain corner and edge sites, a relatively large number of nuclei will be able to form at small undercooling and in short periods of time. In a coarse-grained specimen, relatively few nuclei will be formed under comparable conditions; these factors influence both the amount and the morphology of the ferrite formed.

In a plain carbon steel, the growth of ferrite is dependent on the overall carbon content of the steel, and on this carbon's ability to diffuse away from the interphase boundary. Over the period of the transformation, the interaction between the driving force for the transformation, the amount of ferrite already formed and the carbon level in the remaining austenite leads to an "S" curve when fraction transformed is plotted against time. This form of curve is common to all nucleation-and-growth transformations and can be described using the following equation, commonly known as the Avrami equation:[48]

$$y = 1 - \exp(-kt^n) \qquad \textit{Eq. 2.5}$$

where y is the fraction transformed, t is time, and k and n are time-independent constants for the particular reaction.

As the transformation temperature (i.e. degree of undercooling imposed) is varied, the interplay between nucleation rate (as influenced by driving force) and diffusion rate leads to the classic "C" curve on the appropriate time, temperature, transformation (TTT) diagram.[50] Variations in transformation temperature can also dramatically affect the morphology of the ferrite that results from the reaction.

2.3.4 The Morphological Classification of Ferrite

As the γ-to-α transformation temperature is forcibly lowered, i.e. the degree of supercooling is increased, so the morphology of the resulting ferrite is changed. Dubé proposed a classification of these morphologies that was later extended by Aaronson,[51] and is illustrated in Fig. 2.13.

2.3.4.1 Grain Boundary Allotriomorphs

At small undercooling, pro-eutectoid ferrite (i.e. ferrite formed above the eutectoid temperature) forms as grain boundary allotriomorphs, which as their name suggests, generally nucleate at austenite grain boundaries. As is also suggested by the name (the word "allotriomorph" refers in this case to an outward form that does not display the symmetry of the internal structure), allotriomorphic ferrite does not have regular boundaries with the parent austenite grains, but rather is usually equiaxed or lenticular (lentil-like) in shape since it tends to grow preferentially along the grain boundary on which it was nucleated. This is the first morphology to be found, whatever the degree of undercooling and for any composition; at small undercooling it is the predominant form, and results in an equiaxed ferrite structure. Grain boundary allotriomorphs nucleate with a Kurdjumov-Sachs orientation relationship with one of the two parent grains:

$\{111\}_\gamma // \{110\}_\alpha$

$<110>_\gamma // <111>_\alpha$

But also grow into the other grain, with which they will usually have a random association.

2.3.4.2 Widmanstätten Side Plates and Sawteeth

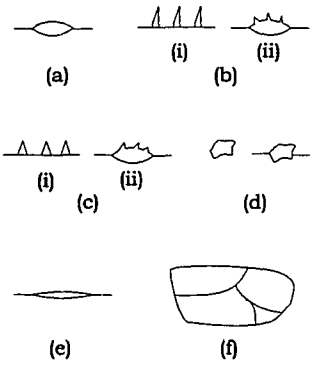

Fig. 2.13 Morphological classification of ferrite colonies: (a) grain boundary allotriomorph; (b) Widmanstätten plates, (i) primary, (ii) secondary; (c) Widmanstätten sawteeth, (i) primary, (ii) secondary; (d) idiomorphs; (e) intragranular Widmanstätten plate; (f) massive ferrite.[33]

At larger undercoolings, there is a greater tendency for ferrite to grow into the parent grains as plates. Laths (narrow plates) of ferrite grow both from clean austenite grain boundaries and from protuberances on pre-existing colonies of grain boundary ferrite. These are known, respectively, as primary and secondary Widmanstätten side plates. The reason for this transition from grain boundary ferrite at lower transformation temperatures is not fully understood, but Aaronson et al.[52] have suggested that it occurs because the relative mobility of coherent or semicoherent boundaries decreases as the temperature is reduced, whereas that of incoherent interfaces increases; thus, there is an increased tendency for plate-like morphologies at larger undercooling. Widmanstätten side plates become finer with increasing undercooling, and are encouraged by large austenite grain sizes, which prevent the impingement of the earlier-forming grain boundary allotriomorphs. Primary and secondary Widmanstätten sawteeth may be regarded as an intermediate morphology between grain boundary allotriomorphs and primary and secondary Widmanstätten side plates.

2.3.4.3 Intragranular Idiomorphs

Idiomorphic ferrite has an irregular equiaxed or polygonal morphology, and tends to form intragranularly, presumably at inclusions and other favoured sites. The term "idiomorph" in this case refers to an outward form that reflects inward symmetry.

Whether or not intragranular precipitation of ferrite is observed depends to a large extent on the austenite grain size. In fine-grained specimens, carbon rejected as ferrite forms on grain boundaries will rapidly raise the carbon concentration in the centres of the grains, increasing the supersaturation and making nucleation even more difficult. In the coarse-grained case, however, this increase in supersaturation will be much less marked and so there will be a greater possibility of ferrite forming at the less favourable intragranular sites.

2.3.4.4 Massive Ferrite

Massive transformations occur at large undercooling and happen very rapidly through the movement of incoherent (high energy) boundaries, which can move at speeds of up to 20 mm s^{-1}.[54] The transformations exhibit nucleation and growth characteristics, and although these are not shear transformations, the mechanism responsible is thought to involve shear-like movements. The microstructures produced by massive transformations often contain large patches of grains with irregular boundaries surrounded by areas with a mixture of planar and curved boundaries. No simple orientation relationships between product and parent matrices are known for this kind of transformation. Since massive transformations occur so rapidly, they are not found in medium or high carbon steels, in which there is insufficient time for enough carbon to diffuse out of the austenite to prevent the formation of martensite.

2.4 The Plastic Deformation of Steel in the Two-Phase Region and its Effect on the Austenite-to-Ferrite Phase Transformation

When metallic structures are plastically deformed, between ~2 and 10% of the energy expended in achieving that deformation remains in the material as crystalline defects.[55] However, plastic deformation in metals is not accommodated uniformly in the microstructure, particularly when more than one phase is present, and therefore the distribution of these faults is also inhomogeneous. The effect of deformation on a diffusional transformation as a result of these defects is essentially two-fold. Firstly, on a simplistic level, deformation increases the number of preferential nucleation sites available

in the material by increasing the number of dislocations, thereby accelerating nucleation. Secondly, deformation aids diffusion through the parent lattice as dislocation lines act as diffusion 'pipes': the greater the number of dislocation lines, the greater the total 'surface area' available for relatively easy diffusion and therefore the faster the progression of diffusion-controlled growth. Umemoto and Tamura[56] have shown, by calculation, that the ferrite growth rate is only slightly enhanced by straining and that the greater effect of deformation on the transformation is its effect on the ferrite nucleation rate. The mechanisms described in the following pages therefore focus on this phenomenon.

The remainder of this section is split into two subsections, the first gives a brief introduction to the plastic deformation of metals in general, and focuses in particular on steel in the vicinity of the two-phase region. The second discusses in more detail the effect of deformation on the austenite-to-ferrite phase transformation.

2.4.1 The Plastic Deformation of Steel in the Two-Phase Region

The behaviour of a single pure metallic crystal subjected to plastic strain is largely controlled by the dislocation density that exists in the crystal at a given point during that deformation, and by the way that those dislocations are distributed; these parameters are controlled by the crystal's stacking fault energy (SFE).[57] In materials with low SFE, such as austenitic stainless steels, cross-slip is relatively difficult and dislocations are therefore usually dissociated into partials, and have low mobility; hence recovery is slow. In this case, a high density of fairly homogeneously distributed dislocations is produced during deformation. Conversely, in materials with high SFE, such as aluminum and body centred cubic (BCC) iron, dislocation cross-slip is relatively easy and recovery therefore much quicker. Plastic deformation of these metals results in a comparatively low dislocation density that is distributed in a more heterogeneous manner.

However, since the mechanisms that control the production, movement and removal of dislocations within individual grains are thermally activated, the density and distribution of dislocations are also strongly affected by the temperature at which the deformation occurs. At elevated temperatures, softening processes such as recovery and recrystallisation[58] are often able to keep pace with the production of dislocations in

response to straining. In this case, the resulting dislocation density will be relatively low. At lower temperatures and/or higher strain rates, on the other hand, the dislocation density will increase for a given applied strain because the aforementioned recovery mechanisms can no longer keep pace with the deformation.

In polycrystalline aggregates, the situation is even more complex. Uri and Wain[59] found that, in coarse-grained high purity aluminum, the tensile elongation in different parts of the aggregate could vary by a factor of 10; it could reasonably be assumed that the dislocation density would vary in a commensurate manner. This study found that strain not only varied from grain to grain, but also that strain could vary markedly within a single grain. If a neighbouring grain had deformed more than the first, then the strain in the latter near the common boundary was usually greater than that at the centre of the grain. If, on the other hand, the neighbouring grain had deformed less, then the strain in the first grain near the boundary tended to be less than that at its centre. It is important to note that strain is continuous across grain boundaries, although there are often steep strain gradients in such areas, and that these large gradients mean that the boundary can have considerable influence over deformation even significant distances away from it.

When steels are deformed at low strain rates in the single-phase austenite region (as can be the case during the unbending operation), deformation occurs both by slip, as would occur at room temperature, and by grain boundary sliding: i.e. essentially by a creep mechanism. As the temperature is raised and the strain rate lowered, the amount of strain taken up by grain boundary sliding is increased, although slip within the grains is still the process that dictates how the deformation as a whole progresses.[60] Slip is the controlling process because shearing becomes less limited to the grain boundaries as deformation advances, and therefore the behaviour of the material is ultimately controlled by slip occurring in a narrow region on either side of the boundaries. However, if (a) the strain rate is raised and the temperature lowered (as can also be the case during the unbending operation), and/or (b) precipitates are formed at grain boundaries, it has been found that much less strain is accommodated by grain boundary sliding and deformation progresses almost exclusively by straining of the bulk material. With respect to point (b), it should be noted that precipitates at grain boundaries often pin said boundaries, allowing deformation

to concentrate in the boundary regions where precipitate free zones frequently exist. Thus an effect opposite to that initially quoted can be observed.

When steels are deformed in the two-phase region, things are, predictably, complicated still further. When an alloy contains two or more ductile phases, a very approximate idea of the alloy's overall mechanical properties can be obtained by calculating a weighted mean of the components, using the rule of mixtures.[47] Thus, if we assume that each phase is subjected to equal stress, we can write the average strain, ε, in a two-phase alloy, in terms of the volume fractions of the two phases present:

$$\varepsilon = \varepsilon_1 f_1 + \varepsilon_2 f_2 \qquad \textit{Eq. 2.6}$$

where f_1 and f_2 are volume fractions, and ε_1 and ε_2 are the respective strains. However, in order to be able to calculate anything from this equation, we need to be know the relative strengths of the phases concerned.

As was suggested in section 2.2.2.1, there is a clear strength differential between austenite and ferrite. This difference was observed by Wray,[32] and is shown in Fig. 2.14, which plots flow stress versus temperature for an Fe-0.24Si alloy. Extrapolation of the curves formed respectively by austenite and ferrite shows a strength differential between the two phases that decreases with decreasing temperature, as has been calculated by Simielli.[61] Wray also found a distinction in the work hardening coefficients, n (= $d\sigma/d\varepsilon$), for the two phases; the n values observed were 0.14 and 0.3 for ferrite and austenite, respectively. The lower value for ferrite supports the statement made above with regard to the influence of SFE on dislocation density—recovery is easier in ferrite because it has a BCC atomic

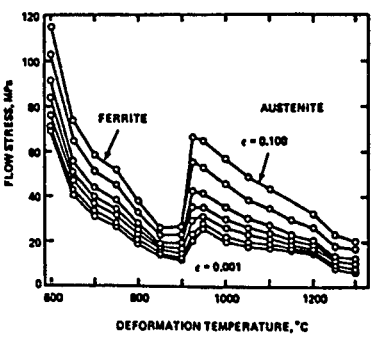

Fig. 2.14 Flow stress v. temperature for an Fe-0.24%Si alloy showing the relative strengths of ferrite and austenite.[61]

arrangement; therefore work hardening is not as marked in this phase as it is in austenite. The speed of dynamic recovery in ferrite also means that the competing softening process of dynamic recrystallisation rarely occurs in this phase, whereas it readily does so in austenite.

Observations of micro-hardness in deformed phases in brass[62] and Al-Mg alloys[63] have shown that when two phases are deformed together, the softer phase absorbs a much larger proportion of the strain in the early stages of straining, while after further deformation, the phases deform to practically the same extent. This was found to be the case unless the volume fraction of the hard phase was less than about 30%, where the softer phase would take more of the deformation. In these experiments, strain was found to be continuous across the interphase boundary, and consequently in the early stages of deformation, the harder phase received more strain in this area than it did further away from the interface and the softer phase received less. Finally, and perhaps most pertinently for the present work, in an investigation that used stainless steels in the γ-plus-δ ferrite two-phase region at temperatures between 1,000 and 1,200°C, Al-Jouni and Sellars[64] observed that the ferrite carried a significantly larger proportion of the applied strain than austenite when its volume fraction dropped to 30% (the lowest that they examined). It might reasonably be assumed that this trend would continue as the ferrite content is reduced further. When there was more than 50% ferrite present, the authors noted that both phases deformed to the same extent, although the sum of the strains taken up by the two phases was less than the total strain applied because of the contribution of interphase boundary sliding.

2.4.2 Deformation and the Kinetics of the Austenite-to-Ferrite Phase Transformation

Much, but not all, of the work that has been performed to date on the effect of deformation on the austenite-to-ferrite transformation has focused on its impact on the controlled rolling of steel. Therefore the strains and strain rates used have, in many cases, been much larger than those found in continuous casting. However, it has not been shown that the mechanisms proposed for ferrite formation in these studies are invalid for the

lower strain rates that we are concerned with here, so this related work is presented in the following sections alongside work that, prima facie, appears more relevant.

2.4.2.1 Suggested Mechanisms for the Effect of Strain on Ferrite Formation

The increase in ferrite nucleation rate per unit volume of austenite caused by deformation is the result of several factors; these include:

1. the increase in γ grain boundary surface area that results from grain elongation;
2. the increase in the ferrite nucleation rate per unit grain boundary area;
3. the formation of additional nucleation sites such as annealing twin boundaries, deformation bands, cell walls, etc.

The first of these factors is fairly self evident and requires no further explanation. The second and third, however, are a little more involved and hence are elaborated upon in the following paragraphs.

Deformation has been shown to dramatically increase the number of ferrite grains nucleated per unit austenite grain boundary area,[65] and a number of explanations have been proposed to account for this effect, none of which necessarily operate alone. Sandberg and Roberts,[66] as a result of a study that used hot compression testing to simulate rolling ($\dot{\varepsilon} = 2\ s^{-1}$), suggested that deformation must produce nucleation sites on grain boundaries that have about the same potency as grain corners or edges. Two candidate scenarios were presented, one related to bulges in grain boundaries, another involving nucleation on subgrain boundaries with growth limited by precipitation of Nb(C, N).

In the case of the former mechanism, ferrite was presumed to nucleate on regions of the austenite grain boundary with locally sharpened curvature (bulges). Such inhomogeneities often form as a precursor to dynamic recrystallization and the authors contended that they might appear even if the temperature were below T_{nr} (the temperature below which recrystallization cannot occur); these sites were thought to be particularly effective in promoting ferrite nucleation because they are plentiful. Umemoto et al.[65, 67] have presented a similar mechanism; in this case though, the inhomogeneities on the

austenite grain boundaries are ledges or steps as shown schematically in Fig. 2.15. If ferrite nucleates in the corner of such a feature then, say the authors, the activation energy for nucleation is reduced by a factor of around θ/π, as depicted in the figure.

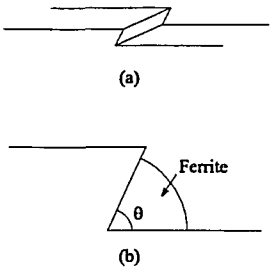

Fig. 2.15 Schematic representation of (a) a ledge on an austenite grain boundary and (b) ferrite nucleation at such a ledge.[45]

Deformation substructures have also been shown to act as effective ferrite nucleation sites. Sandberg and Robert's latter scenario suggests that the growth of ferrite grains nucleated on austenite subgrain boundaries could be limited by the strain-induced precipitation of Nb(C, N). Were this the case, then other potential nucleation sites would be 'shielded' from destruction by these previously nucleated grains, and hence the measured nucleation rate would increase. The authors did not reach any strong conclusions with regard to this mechanism as the effectiveness of subgrain boundaries in nucleating ferrite was thought to be unclear.

As a result of a similar investigation, although this time using a laboratory-scale rolling mill, Amin and Pickering[68] suggested that the multiple nucleation of ferrite at and near the deformed austenite grain boundaries may have resulted from a type of substructure. In this model, illustrated schematically in Fig. 2.16, a subgrain network is developed (Fig. 2.16(a) and (b)) during deformation. This substructure is finer closer to the austenite grain boundary because of the dramatic strain gradient present in such areas. Precipitates then form on this network (Fig. 2.16(c)), and it is these that act as ferrite nucleation sites (Fig. 2.16(d), (e) and (f)). It is notable that, in many cases in this study, bulges were not observed on austenite grain boundaries as had been noted by Sandberg and Roberts. Amin and Pickering suggested that the increased rate of ferrite nucleation in these areas must therefore be due to another mechanism, such as local lattice mismatch.

2.4.2.2 The Effect of Strain Rate

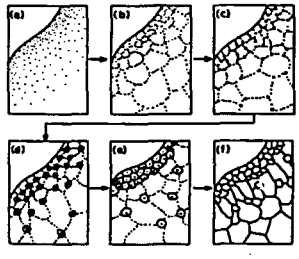

Fig. 2.16 Schematic representation of ferrite nucleation at austenite subgrain boundaries (see text for details).[68]

Mintz and Jonas[27] have examined the effect of strain rate in hot compression tests on the production of deformation-induced ferrite for strain rates of 3×10^{-2}, 3×10^{-3}, and 3×10^{-4} s^{-1}, over the temperature range 600 to 1,100°C—ranges representative of those encountered during the unbending operation. On examination of the flow curves in the temperature region 610 to 750°C, the authors found that at the lowest strain rate, the strain to peak stress *decreased* with decreasing temperature. This was shown to be related to the formation of deformation induced ferrite at higher temperatures, and to spheroidation at lower temperatures; more normal stress-strain curves were found at the higher strain rates. Strain rate was also found to affect the dynamic recovery of ferrite; the lowest strain rate used here allowed full recovery and/or recrystallization to occur, while higher strain rates did not. It was therefore suggested that raising the strain rate could improve the ductility of the steel by work hardening the ferrite and thereby reducing the strength differential between this softer phase and the austenite. This would to some extent limit the strain concentration that occurs at lower strain rates.

The effect of strain rate was also investigated by Essadiqi and Jonas[69, 70 & 71] who found that, at a given temperature, increasing the strain rate accelerated ferrite nucleation. They found that increasing the strain rate from 7.4×10^{-4} to 7.4×10^{-1} s^{-1} raised the nucleation rate by about three orders of magnitude in a Mo steel at 800°C, and that the increase in ferrite nucleation rate was greatest when straining was applied during transformation, rather than before transformation as a 'prestrain'. They also found that increasing the strain rate considerably improved the homogeneity of the ferrite microstructure and led to very fine grain sizes (≈2 μm).

2.4.2.3 The Effect of Strain on the Ar_3 Temperature

Since the Ar_3 temperature is a value that expresses the hysteresis encountered in the austenite-to-ferrite transformation, any increase in the number of preferred sites for the nucleation of the latter phase is likely to have some effect on this figure. As was mentioned in section 2.2.2.1, Crowther and Mintz found, in relatively early work, that during deformation, thin films of ferrite would form above the static Ar_3 and up to the Ae_3.[33] Significant thickening of these films was only observed to occur below the static Ar_3. Cardoso and Yue[43, 44] also noted that thin ferrite films formed in steels deformed between the Ae_3 and the undeformed Ar_3, while Pandi and Yue[72, 73] found that increasing the strain applied prior to reaching the static Ar_3 temperature, at constant cooling rate and strain rate, resulted in an increase in the observed Ar_3 (that applicable when the material had undergone a given amount of deformation).

Chapter 3

Experimental Arrangements

3.1 Experimental Material

The steel used in the course of this work was a C-Mn grade supplied by British Steel in the form of hot rolled plate. The chemical composition of this steel is displayed in Table 3.1.

Table 3.1 Chemical composition (in weight %) of the experimental material.

C	Mn	Si	P	S	Sol. Al	N
0.1	1.43	0.31	0.016	0.003	0.03	.0056

3.2 Mechanical Testing and Related Equipment

Hot compression and hot tensile tests were carried out using two separate servohydraulically actuated testing arrangements, one configured for each type of testing regime. The material used for the tooling, and the furnace and temperature control

equipment, are essentially identical for both arrangements, so these items are described first in sections 3.2.1 and 3.2.2, respectively. However, the two testing machines differ in their configurations and are driven by different control arrangements; these machines are therefore described separately alongside the respective tooling arrangements in sections 3.2.3 and 3.2.4.

3.2.1 Tooling Materials

During hot working experiments, significant parts of the tooling are often heated in the furnace, along with the specimen, in order to reduce any temperature gradient in the sample. The material used for these tools must therefore be able to simultaneously withstand both the high temperatures and the often considerable stresses that are encountered in such environments. Candidate materials must possess a combination of high melting point, high strength, good creep resistance and the absence of a phase transformation in the hot working temperature range.

An alloy that fulfils these criteria, and has consequently been used in both the compression and tensile tooling in this work is TZM, a molybdenum-based alloy containing a dispersion of 0.5% Ti and 0.08% Zr oxides (hence the initials TZM). In addition to the above specifications, this alloy is resistant to recrystallization and softening,[74, 75] and is relatively easy to machine. However, at temperatures above 550°C TZM oxidises very rapidly in air and so experiments undertaken at elevated temperatures must be performed in an inert atmosphere; TZM has been shown to offer a long service life under conditions controlled in this manner.[74] Compression tools fabricated from TZM have been used successfully in hot working experiments by Simielli,[61] Pandi[72] and Zarei-Hanzaki,[76] amongst many others. Similarly, tensile tools made from TZM have been used successfully by many workers including Cardoso,[44] Guillet[77] and Trudel.[78]

3.2.2 Furnace and Temperature Control

The thermal cycles employed in this work were imposed using Research Incorporated radiant furnaces equipped with 16 kW power supplies and linked to Micristar digital controller/programmers. Heat is generated in each furnace by four tungsten

filament lamps, and is reflected into the centre of the furnace chamber (where the specimen is located) by mirror finished elliptical reflectors. The controller/programmers use a feedback control circuit to maintain the desired temperature, which in this case was measured using a chromel-alumel (K-type) closed tip thermocouple placed in contact with the surface of the specimens at the centre of the gauge length.

In order to provide the necessary inert atmosphere that was mentioned in section 3.2.1, the specimen and anvils were, in both the compression and tensile cases, enclosed in a quartz tube that was sealed with O-rings at either end. A continuous flow of 'prepurified grade' argon (99.998% pure) was injected into this tube in order to ensure a positive pressure of this noble gas at all times and therefore minimise the chance of any oxygen reaching the tools.

3.2.3 Compression Testing Apparatus

The compression testing apparatus (Fig. 3.1) is built around an MTS (Material Test System) Model 810 axial testing machine, which consists of a load frame, rated at 25 kN, and a closed loop hydraulic power supply with a computerised control system. A hydraulic actuator, in this case mounted at the bottom of the load frame, generates force which, having been applied to the specimen, is measured by a load cell mounted at the upper end of the frame. Vertical displacement is measured using a linear variable differential transformer (LVDT) which is mounted on a shaft that is connected to the hydraulic piston; the LVDT communicates this positional information to the feedback control loop. Two important features of the compression tooling itself are the quenching lever and the sample exit, which is located in the lower O-ring. When the intended strain has been reached, the testing program instructs the machine to release the load, and the sample can then be dislodged using the quenching lever in order that it may fall out of the furnace, via the sample exit, and into a waiting container of water. This happens in around 1 s after the end of the test and is therefore quite an effective method of 'freezing in' the microstructure that existed at that time.

The computer control system is used to generate commands, record data, and perform real-time decision making during tests. It consists of a Digital PDP-11

microcomputer, running the RT11 operating system, that interfaces the servohydraulics through an MTS 468.20 Test Processor. The user may communicate with the PDP-11 via a Digital VT240 terminal. Management of the hydraulic power supply and manual adjustment of actuator position is performed using an MTS 413.81 Master Controller.

The mechanical testing regime used in the present work on this apparatus was programmed in MTS 773 BASIC V02.09—a language very similar to ANSI BASIC, but with added features that allow access to specific MTS functions. A listing of the program, which was written by Zarei-Hanzaki,[76] is included in Appendix I. At run-time, the software asks for information such as the specimen height and diameter, and the intended nominal strain and strain rate. It uses these figures to determine the required actuator position for each point in the test, and to calculate the true stress and strain (see section

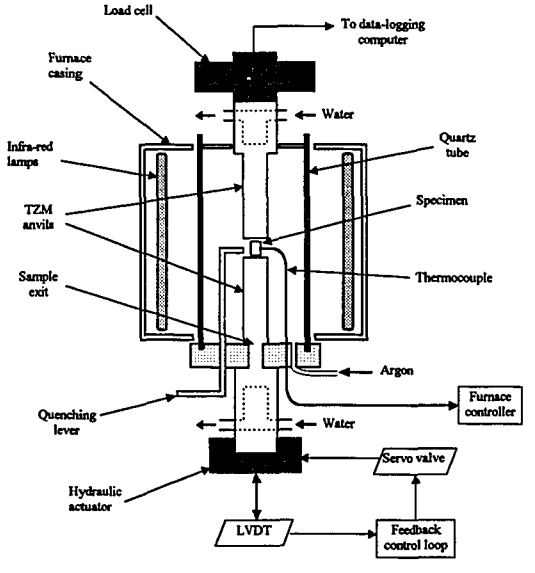

Fig. 3.1 Schematic cross-section through the compression testing equipment.

3.3.2) for output at the end of the experiment. The data displayed after the test may be saved to a file on the PDP-11's floppy disk drive, and a separate program may then be used to transfer the data to a PC running DOS.

3.2.4 Tensile Testing Apparatus

The tensile testing apparatus (Fig. 3.2) is built around an MTS axial testing machine, which consists of a load frame rated at 100 kN and a closed loop hydraulic power supply with a computerised control system. A hydraulic actuator, in this instance mounted at the top of the load frame, generates a force which, having been applied to the specimen, is measured by a load cell mounted at the lower end of the frame. As with the compression set up, vertical displacement is measured using an LVDT which is mounted on a shaft that is connected to the hydraulic piston. Perhaps the most important feature of

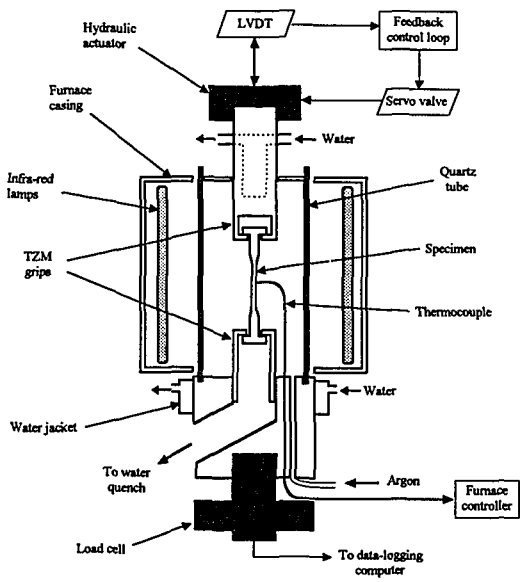

Fig. 3.2 Schematic cross-section through the tensile testing equipment.

the tensile tooling arrangement, which was designed by Cardoso,[44] is the lower grip configuration, which allows the lower portion of the sample to exit the furnace immediately that fracture occurs. This allows for half of the sample to be quenched for subsequent metallographic analysis, while the other half may be furnace cooled in an inert atmosphere so that the fracture surface remains free of oxide, thus facilitating later microscopic examination.

The control system in this case is a modern MTS TestStar system that the user can communicate with via either a personal computer running the IBM OS/2 operating system, or the system's 'Load Unit Control Panel'—a moveable, free-standing unit that allows the operator to control the actuator position, reset the instruments, and run pre-programmed deformation schedules without needing to be close to the PC.

The TestStar system allows simple deformation routines to be defined by the use of the machine's built-in ramping and periodic functions exclusively. However, more complex regimes, as are required in this work, can only be accommodated using the software's 'playback' function, which allows the machine to 'playback' a previously prepared datafile that contains a list of times and actuator positions for the computer to follow. This playback facility is invoked after the machine's in-built functions have been used to move the actuator so that it is in a position to begin the test proper. All the information for a given test is contained in a file that the TestStar system terms a 'procedure'. This file holds a large amount of information, including the procedure name, approach instructions, playback file to use, and data file options, and serves as the machine's overview of the test.

The playback datafiles used this work were intended to give constant true strain rate tests (see section 3.3.2), and, since smooth actuator movement requires the definition of a large number of finely-spaced datapoints, were generated using a computer program. The program, which was created by Dr T. Maccagno and is written in BASIC, asks for the intended strain rate and the gauge length, and then generates the appropriate set of numbers, which it saves in a file, ready for playback. A listing of this program is included in Appendix II.

The output datafile written by the TestStar software after each test provides force and extension information, not true stress and strain, as is the case with the compression apparatus. The tensile data were therefore treated using a standard commercial spreadsheet package in order to extract the desired figures. Instantaneous true strain, ε, (see section 3.3.2) was calculated using:

$$\varepsilon = \ln\frac{l}{l_0} = \ln\left[\frac{(l_0 + \Delta l)}{l_0}\right] \qquad \textit{Eq. 3.1}$$

where l is the instantaneous gauge length, l_0 is the initial gauge length and Δl is the extension, which is all assumed to occur within the gauge length. Instantaneous true stress, σ, is simply the applied force divided by the instantaneous area, and was calculated from constant volume considerations using:

$$\sigma = \frac{4F(l_0 + \Delta l)}{\Pi l_o d_0^2} \qquad \textit{Eq. 3.2}$$

where F is the applied force and d_o is the original gauge diameter.

Having measured the initial gauge diameter and final fracture surface diameter, percentage reduction in area (%RA) was calculated using:

$$\%RA = 100\left(1 - \frac{d_f^2}{d_0^2}\right) \qquad \textit{Eq. 3.3}$$

where d_f is the fracture surface diameter. The percent elongation was not used as a measure of ductility because, unlike %RA, it is dependent on gauge length—the shorter the gauge, the greater is the fraction of the total elongation that occurs in the neck, and so the higher is the calculated value of percentage elongation for a given level of ductility.

3.3 Experimental Methods

3.3.1 Sample Preparation

Both the compression and the tensile specimens were machined from the as-received plate with their longitudinal axes parallel to the rolling direction. The

compression specimens were cylindrical and measured 11.4 mm high by 7.6 mm in diameter—giving an aspect ratio of 1.5, which has been shown to promote homogeneous deformation.[79]

The dimensions of the tensile specimens were, of course, a little more complicated and are illustrated in Fig. 3.3. The gauge length of these samples was 16 mm and the ratio of gauge length to diameter was 4:1, as is specified in the ASTM standard for tensile specimen preparation.[80] However, the ASTM standard assumes that the reduced diameter section is somewhat longer than the gauge length and that the gauge is distinguished by the use of an extensometer—an operation that is very difficult in the case of high temperature testing and that consequently has not been attempted here. In these tests, therefore, the gauge is assumed to occupy the entire length of the reduced section. The result of this is that, while the aspect ratio has been preserved, some inaccuracies will have been incurred due to the complex stresses that will have been present at the ends of the gauge length, where the sample would ideally have been in uniaxial tension.

During the compression tests, thin sheets of mica (50 to 80 μm thick), separated by a layer of boron nitride powder, were placed between the faces of the compression specimens and the anvils in order both to maintain uniform deformation, and to avoid quenching problems due to sticking. The loaded surfaces of each tensile sample were lubricated in the same way, although in this case the reason for the lubrication was purely one of preventing the sample from sticking to the grip and thereby evading an immediate quench upon fracture.

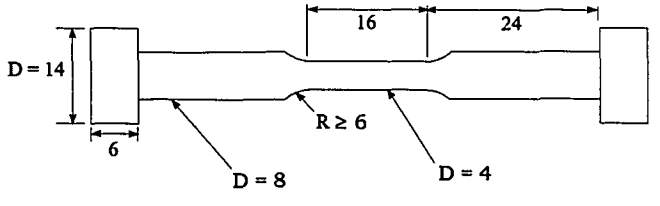

Fig. 3.3 Tensile specimen configuration, dimensions in mm.

3.3.2 Constant True Strain Rate Testing

All the mechanical tests that were undertaken as part of the present work were performed under constant *true* strain rate conditions. Processes that occur in metals during high temperature deformation are rate sensitive, so testing at constant crosshead speed (i.e. varying true strain rate) complicates matters considerably. Below is a brief explanation of what is meant by true strain, and how in general terms a deformation schedule incorporating constant true strain rate may be created.

In uniaxial deformation processes that involve only small changes in a specimen's dimensions, it is sufficient to express the degree of the deformation in *engineering* strain, e, i.e. as the change in length referred to the original length:

$$e = \frac{\Delta l}{l_0} = \frac{1}{l_0}\int_{l_0}^{l} dl \qquad \textit{Eq. 3.4}$$

where l is the instantaneous gauge length, Δl is the change in gauge length, and l_0 is the original length. One can see that a constant engineering strain rate would require a constant crosshead velocity. However, the above theory becomes less valid as the degree of straining is increased; in these situations a second way of expressing strain is required, that of *true* strain, ε. According to this definition of strain, the change in length is referred to the *instantaneous* gauge length, rather than the original length; since the instantaneous gauge length is constantly changing, these values must be summed by integration:

$$\varepsilon = \sum \frac{l_1 - l_0}{l_0} + \frac{l_2 - l_1}{l_1} + \frac{l_3 - l_2}{l_2} + \ldots \qquad \textit{Eq. 3.5}$$

or

$$\varepsilon = \int_{l_0}^{l} \frac{dl}{l} = \ln \frac{l}{l_0} \qquad \textit{Eq. 3.6}$$

Differentiating Eq. 3.6 with respect to time and rearranging, we can obtain an expression for the crosshead velocity in terms of the instantaneous gauge length and the true strain rate, $\dot{\varepsilon}$:

$$\frac{dl}{dt} = l\dot{\varepsilon} \qquad \textit{Eq. 3.7}$$

However, we need to be able to tell the testing machine *where* to put the crosshead at a given juncture, so we must integrate Eq. 3.7 with respect to time. By first substituting for l from Eq. 3.6, then remembering that $\varepsilon = t\dot{\varepsilon}$, and finally integrating and simplifying, we obtain:

$$l = l_0 \exp(t\dot{\varepsilon}) \qquad \textit{Eq. 3.8}$$

Since computers cannot deal directly with continuous functions, the time for the test must be split into increments and a calculation performed for each of these; hence a list of times and positions can be generated, using Eq. 3.8, for the actuator to follow.

As was explained in sections 3.2.3 and 3.2.4, the two computer control systems used in this work deal with these datapoints in slightly different ways. Nevertheless, the theory behind the generation of these points is identical, as outlined in the preceding paragraphs.

3.3.3 Thermal Cycles and Deformation Schedules

The thermal cycles and deformation schedules imposed during the compression phase of this work, which was largely completed prior to the present author's involvement, were intended to allow examination of the effect of prior austenite grain size, degree of undercooling, strain rate, and degree of straining on the formation of DIF. Static tests were also performed, by the present author, using the same compression specimens and the same apparatus as used in the compression tests proper, in order to allow comparison of the static and dynamic cases.

The thermal cycles used are illustrated in Fig. 3.4. The samples were first heated to either 920 or 1,200°C to give fine (25μm) or coarse (200μm) austenite grain sizes, respectively; the heating rates employed were 5 minutes to reach 600°C from ambient temperature, and then a further 15 minutes to pass from 600 to 920 or 1,200°C, depending on the particular experiment. Samples were held at these soaking temperatures for 15 minutes and then cooled at 1°C s^{-1} (a rate similar to the mean found in continuous casting)

to test temperatures ranging from 760 to 1,000°C. At this point they were held for 5 min to allow the temperature throughout the specimen to equalise, and then deformed and finally quenched. For reasons that will be explained momentarily, most of the tests were performed between 760 and 840°C. In the case of the static tests, samples were held at test temperatures for times equivalent to those encountered in the dynamic tests, and were subsequently quenched in the same manner.

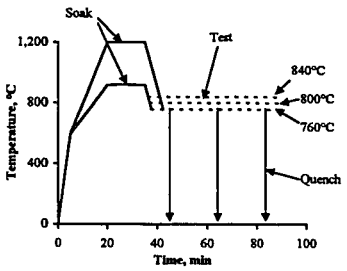

Fig. 3.4 *Schematic diagram of the thermal cycles employed.*

The Ae_3 temperature for the steel under investigation, evaluated using the ThermoCalc program,[81] was 841°C. The (undeformed) Ar_3 temperatures, under conditions similar to those used here, for two similar steels used in previous work were 744 and 735°C.[33, 82] It was assumed that the present material would exhibit similar properties in this respect and it is for this reason that the majority of mechanical tests were carried out at temperatures between 760 and 840°C—since deformation induced ferrite would be expected to form in this temperature range. The equilibrium volume fractions across the range of testing temperatures, again evaluated using the ThermoCalc program, are displayed in Table 3.2.

Table 3.2 Calculated equilibrium volume fractions of ferrite across the range of testing temperatures.[81]

Temperature, °C	840	820	800	780	760
Volume fraction ferrite, %	0	0.22	0.43	0.58	0.68

Compression specimens were strained at constant true strain rates of 3×10^{-2}, 3×10^{-3}, and 3×10^{-4} s^{-1} to final nominal true strains of 0.05, 0.15, 0.4, and 0.8, and were quenched at the end of each test using the arrangement described in section 3.2.3.

The tensile portion of this work was intended to allow the information gained on the development of DIF during compressive straining to be related to the tensile hot ductility found in the same steel under similar conditions. Tensile specimens were subjected to the thermal cycle designed to produce a coarse prior austenite grain size (please see next section for explanation as to why the fine-grained cycle was not included). The samples were then strained at the same strain rates as those used in compression until failure, whereupon, as was described in section 3.2.4, the bottom half of each specimen was quenched, while the top half was furnace cooled in preparation for fractographic examination.

3.3.4 Temperature Control Problems During Tensile Testing

When the initial tensile results were plotted, few clear trends were evident in the data, and as a result, a careful check of the experimental conditions was performed. Three thermocouples were positioned at the same location in the furnace used for tensile testing, and the furnace was heated to around 800°C using its manual controls. The readings from these three thermocouples were then checked against each other in order for the error at this temperature to be calculated. The average of the three readings was taken to be the 'actual' temperature. It was found that the thermocouples agreed to ± 5°C at this temperature; the error for each was recorded. A tensile sample was then placed in the furnace, and the thermocouples fixed at the top, middle and bottom of the gauge length. A number of thermal cycles were then run, using the central thermocouple to control the furnace, in order to assess temperature differences across the sample as each test progressed. It was found that, with the original set-up, the temperature variation across the sample could be as much as 50°C at 840°C, making the previous tests essentially meaningless.

A number of steps were taken to rectify this situation. First, the cooling system was modified to allow the cooling water flow rate to the grips to be varied; the object of

this was to allow the grips to warm up, and thus reduce the thermal gradient along the length of the furnace. Second, the sample was raised in the furnace by using an extension to the bottom grip. These two measures reduced the problem, but did not remove it; it was therefore further decided to reduce the specimen gauge length by half. This final step brought the thermal variation across the sample down, at worst, to around ± 8°C, which was considered acceptable. Note that the specimen dimensions presented in Fig. 3.3 earlier in this chapter are those arrived at *after* the aforementioned changes had been made.

The fine grained specimens initially tested in tension showed no sign of a ductility trough, and based on this fact, and on the fact that large amounts of ferrite had been present in the fine grained compression specimens, it was considered that samples with fine austenite grains would be unlikely to exhibit a significant trough, even when tested at the intended temperature. Due to a lack of material, it was therefore decided that it would be sufficient to repeat the tensile tests only for the coarse grained scenario.

3.4 Microstructural Investigation

3.4.1 Metallographic Preparation

Compression samples were sectioned at their centres, and tensile samples along the tensile axis, using a thin wafering blade where necessary. Both were mounted in Bakelite and ground in the normal manner beginning with 60 and finishing with 600 grit silicon carbide paper. Polishing was performed using 6 μm diamond paste followed by 0.5 μm alumina powder, at which point all specimens were etched using 2% nital. In cases where it was difficult to distinguish the ferrite from martensite, Marder and Benscotter's reagent (10 g sodium metabisulphate in 100 ml of water),[83] which enhances contrast between these two phases, was used after the nital etch.

3.4.2 Quantitative Metallography

Samples were examined using the Leco 2002 image analysis equipment as a means of producing an image on a screen. Prior austenite grain size was then measured using the

mean linear intercept method, whereby the number of grain boundaries intercepted by a line of a specified length placed randomly on an image of the microstructure is counted. This procedure is described in ASTM standard E-112.[84] Ferrite volume fraction was measured by point counting:[83] fifteen fields of 25 points were counted, giving a total count of 375 points. These analyses were all done by hand, because it was found impossible to get repeatable results using computerised image analysis equipment, given the often similar shading of ferrite and martensite.

3.4.3 Fractography

Fractography was performed on the portions of the tensile samples that had been allowed to cool to room temperature in argon (see section 3.2.4) using the JEOL JSM-840A scanning electron microscope (SEM). The microscope was operated in the secondary electron mode with an accelerating voltage of 10 kV and a working distance of 48 mm.[85] Extended working distances such as this give maximum depth of field, which is paramount when viewing fracture surfaces.

Samples were prepared by discarding all but the portion of the specimens within about 15 mm of the fracture surface. These samples were then mounted upright on the microscope's brass sample holder using double-sided carbon tape, ensuring good contact so as to avoid charging of the sample. Fractographs were taken at magnifications varying from 200 to 5,000× using this arrangement.

Chapter 4

Experimental Results Part 1:

The Formation of DIF

For convenience, the results are presented in two separate chapters. The present one covers the factors that influence the formation of deformation induced ferrite, while second deals with the effect that DIF has on the tensile hot ductility. This chapter contains results from both static transformation and compression tests and attempts to trace the effects of factors such as test temperature and strain rate on the austenite-to-ferrite transformation. Chapter 5 contains tensile hot ductility results obtained using the same thermal cycles and strain rates as were used in the compressive case. This second chapter presents ductility curves alongside both qualitative and quantitative microstructural observations.

4.1 Static Transformation Tests

In order to provide a baseline against which to compare the results from the dynamic tests, a significant number of compression specimens were subjected, without

deformation, to thermal cycles identical to those used in the tests in which strain was applied (see section 3.3.3). The results of these 'static' experiments are presented below.

The heat treatments performed at holding temperatures of 840 and 800°C yielded no ferrite, even when specimens were held at temperature over time periods several hours in excess of the 2,940 s taken by the longest dynamic test (carried out to a strain of 0.8 at $3 \times 10^{-4} s^{-1}$, including the 300 s holding period). The ferrite volume fraction is therefore plotted against holding time in Fig. 4.1 only for the case of the specimens treated at 760°C. Avrami-type equations were used to draw curves through the datapoints.

It can be seen from the figure that reducing the prior austenite grain size accelerates the kinetics of the austenite-to-ferrite transformation—i.e. the curve is moved to shorter times. In either case, though, it takes in excess of 10,000 s (about three hours) to approach equilibrium. It is also quite clear that there is significantly more scatter in the fine than in the coarse grained results; this trend was observed consistently in both the static and compressive results, and is discussed further in section 6.1.1.

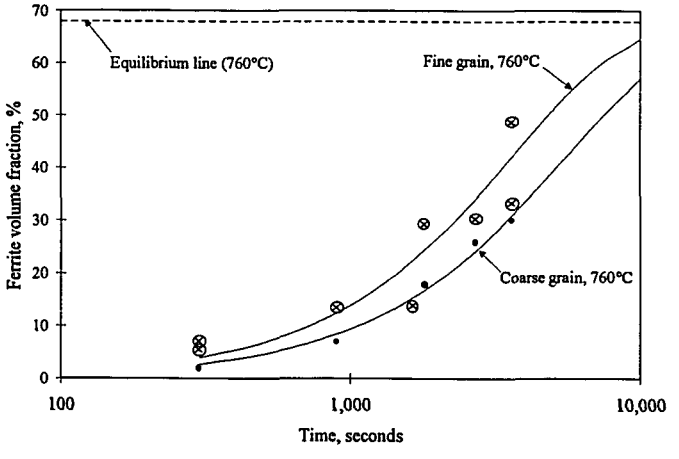

Fig. 4.1 Dependence of ferrite volume fraction on holding time under static conditions.

Examples of the microstructures found in specimens subjected to static heat treatments are presented in Fig. 4.2. As has been mentioned, samples held at 840 and 800°C contained no ferrite; hence a purely martensitic structure was found upon examining these specimens after quenching. Such a structure is illustrated in Fig. 4.2 (a). As has also been mentioned, at a test temperature of 760°C, significant amounts of ferrite were observed in both fine and coarse grained samples after the 1,800 s holding time applied to each of the samples depicted in the figure. Figs 4.2 (b) and (c) show, respectively, the microstructures of coarse and fine grained samples treated at 760°C. One can perhaps most easily see from Fig. 4.2 (b) that, under static conditions at this level of undercooling, the ferrite colonies form exclusively at grain boundaries, and particularly at triple points. It is also notable that there is a substantial variation in ferrite grain size, a phenomenon that indicates the presence of different types of nucleation site, exhibiting different levels of free energy.

4.2 Compression Tests

Before presenting the compression test results, the author would like to draw attention to the fact that the majority of the test data to be presented in this section were provided by Professor B. Mintz of The City University, London, England. The present author repeated several of these experiments in order to confirm the results, and performed the plotting and presentation of the data as they are seen below. These results are supplied as part of this thesis because the data from the static and tensile experiments performed subsequently do not stand alone, and are most valuable when viewed in the light of the compression tests that went before.

4.2.1 Compressive Flow Curves

The first piece of evidence gained from a hot compression test is the flow curve. Much information can be derived from the shapes of these curves; this section outlines some of the trends observed during the course of this work.

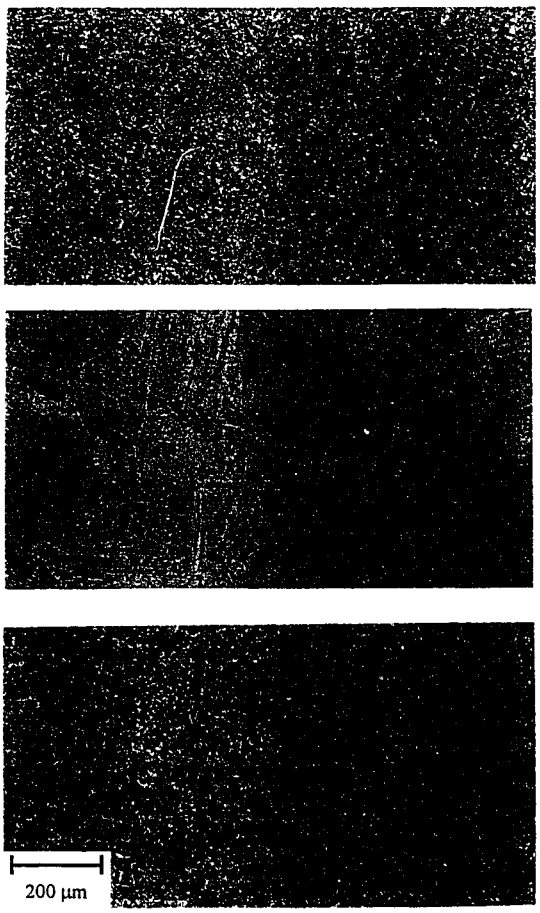

Fig. 4.2 *Microstructures of unstrained samples held for 1800 s: (a) fine grained sample held at 800°C, (b) and (c) coarse and fine grained samples held at 760°C.*

Provided the applied strain was sufficient to reveal enough of the flow curve, all the compression samples displayed true stress/strain plots similar to those shown in Fig. 4.3. It can be seen that the stress increases to a maximum in each case and then falls as further strain is applied. It can also be seen that there is an appreciable effect of strain rate, both before and after the peaks—increasing the strain rate significantly increases the flow stress at all points on the curves.

The existence of one or more maxima in compressive flow curves signifies the action of at least one softening mechanism. Softening mechanisms are important in the present work because they interfere with a material's ability to retain work hardening, and therefore influence the point at which plastic instability sets in in tension. This has a significant effect on tensile ductility. The initiation of softening processes is always dependent on the conditions (e.g. temperature and strain rate) imposed in a given experiment; as the subject is quite involved, the variation of peak stress with temperature, strain rate and prior austenite grain size is plotted and the resulting curves considered in detail in section 6.1.2.2, as part of the Discussion.

4.2.2 Metallographic Investigation

Metallographic samples were prepared from the static and compression specimens, as per the procedure described in Chapter 3, and both qualitative and quantitative observations were made. These are presented below.

4.2.2.1 General Observations: Coarse Grained Samples Tested in Compression

At 840°C at the lower strain rates examined, small volume fractions (≈ 4%) of deformation induced ferrite were found in the coarse grained specimens; ferrite colonies were in the form of continuous bands decorating the prior austenite grain boundaries (Fig. 4.4). While no ferrite formation was observed at the highest strain rate, decreasing the strain rate from 3×10^{-3} s^{-1} to 3×10^{-4} s^{-1} resulted in a thickening of the bands found at these lower rates of deformation (Fig. 4.5).

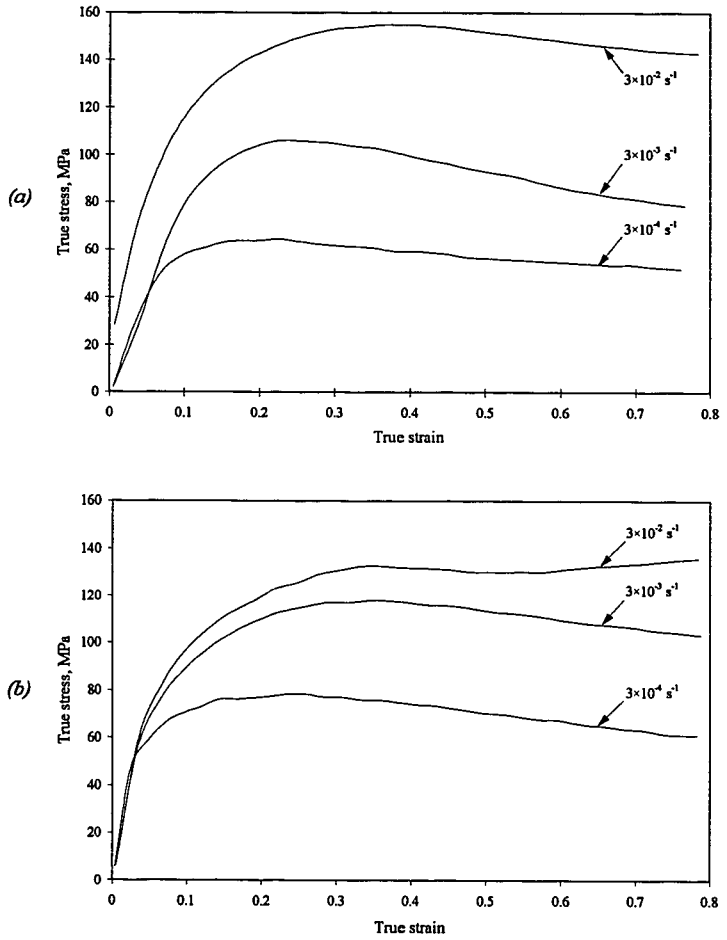

Fig. 4.3 *Typical flow curves for (a) coarse grained specimens tested at 760°C and (b) fine grained specimens tested at 800°C, at each of the three strain rates examined.*

Fig. 4.4 Formation of thin continuous bands of DIF at the austenite grain boundaries. (Coarse grained specimen tested at 840°C at 3×10^{-3} s^{-1}.)

At 800°C, ferrite bands were found at all three strain rates, while reducing the rate of deformation at this temperature again resulted in a thickening of the bands. This may be seen from Table 4.1, which displays the changes in grain boundary ferrite film thickness in the coarse grained case under various conditions. It is notable that at this temperature, thin films of ferrite were observed after nominal true strains as low as 0.05 at the lowest

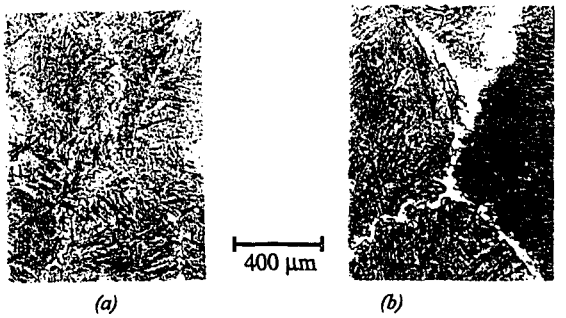

Fig. 4.5 Effect of strain rate on the formation of DIF. (Coarse grained samples tested at 760°C and strained to 0.4 at strain rates of (a) 3×10^{-2} and (b) 3×10^{-4} s^{-1}.)

Table 4.1 Thickness of ferrite at the γ grain boundaries in the coarse grained steel.

		Thickness of ferrite band, μm+			
		Strain, ε			
Temp, °C	Strain Rate, $\dot{\varepsilon}$	0.05	0.15	0.4	0.8
840	3×10^{-3} s^{-1}	-	-	3.5	
800	3×10^{-2} s^{-1}	-	-	3.5	5.0
	3×10^{-3} s^{-1}	-	-	9.0	
	3×10^{-4} s^{-1}	3.0	-	9.0	12.0
760	3×10^{-2} s^{-1}	-	17.0	16.0	20.0
	3×10^{-3} s^{-1}	-	30.0	NV*	NV*
	3×10^{-4} s^{-1}	-	25.0	NV*	NV*

+ Allowance has been made for compressive spread for strains > 0.15.
* Value not taken, as > 25% ferrite can no longer be regarded as a film.

strain rate. This agrees with previous observations,[34] which indicate that thin films of ferrite can form in coarse grained steels at the low strains that are found in the straightening operation.

Samples tested at 760°C contained thicker bands than those tested at the higher temperatures; extensive growth of this second phase had also occurred at triple points. At the lowest strain rate, subgrain formation was apparent, indicating that a considerable amount of recovery had occurred within the ferrite.

4.2.2.2 General Observations: Fine Grained Samples Tested in Compression

At temperatures above 825°C, metallographic examination revealed the presence of very small amounts of DIF in the fine grained material, formed mostly at triple points. Straining at a rate of 3×10^{-2} s^{-1} to 0.4 produced 5% ferrite, where deforming to the same degree at $3\times10^{-4}s^{-1}$ yielded 12% ferrite. At 800°C, however, deformation produced equilibrium volume fractions of ferrite after strains of as little as 0.15 at the lower strain rates tested. In cases in which equilibrium was not reached so quickly, increasing the strain and decreasing the strain rate, as in the coarse grained case, led to larger amounts of

ferrite. Raising the strain rate also generally refined the ferrite structure, but the changes in grain size were small. Table 4.2 shows the influence of strain and strain rate on the ferrite grain size in the fine grained condition.

Referring to the table, it can be seen that finer ferrite was formed at 800 than at 760°C. This observation tallies with the work of Essadiqi and Jonas,[71] who suggested that the refinement found at higher transformation temperatures is due to the larger amount of deformation applied to the γ before transformation begins, resulting in a higher density of ferrite nucleation sites. Referring again to Table 4.2, it is clear that the level of straining imposed also had an effect on the ferrite grain size at 800°C, if not on that found at 760°C. Straining to $\varepsilon = 0.8$ at 800°C caused a refinement in ferrite grain size; the refined grains contained no substructure and were therefore probably the products of recrystallization. At 760°C, at most only partial recrystallization took place; under these conditions, no overall refinement was observed as the strain was increased, see Fig. 4.6.

4.2.2.3 Influence of Grain Size, Strain Rate and Temperature on the Amount of Ferrite Formed in Compression

The effect of grain size, strain rate and temperature on the amount (i.e. volume fraction) of ferrite formed for nominal strains of (a) 0.15, (b) 0.4 and (c) 0.8 is illustrated in Fig. 4.7. The equilibrium volume fraction curve is also shown in each of these figures. Referring to the graphs, it was consistently found that reducing the test temperature (i.e. increasing the undercooling), all other things being equal, increased the amount of ferrite formed. This effect is easiest to see in the coarse grained samples, as the ferrite volume fraction in these cases does not approach equilibrium as quickly as in the fine grained case. The effect of temperature was non-linear—the gradients of the curves increase with the degree of undercooling.

Table 4.2 Influence of strain and strain rate on the as-quenched ferrite grain size in the fine grained samples.

(a) 800°C

	Grain size, μm		
	Strain ε		
Strain rate $\dot{\varepsilon}$, s^{-1}	0.15	0.4	0.8*
3×10^{-4} s^{-1}	-	8*	4.0
3×10^{-3} s^{-1}	5.5*	5.5*	3.0
3×10^{-2} s^{-1}	-	-	3.5

(b) 760°C

	Grain size, μm		
	Strain ε		
Strain rate $\dot{\varepsilon}$, s^{-1}	0.15*	0.4*	0.8*
3×10^{-4} s^{-1}	13	12	12
3×10^{-3} s^{-1}	12	12	12
3×10^{-2} s^{-1}	10	12	12

*Grain size has been corrected for compressive spread.

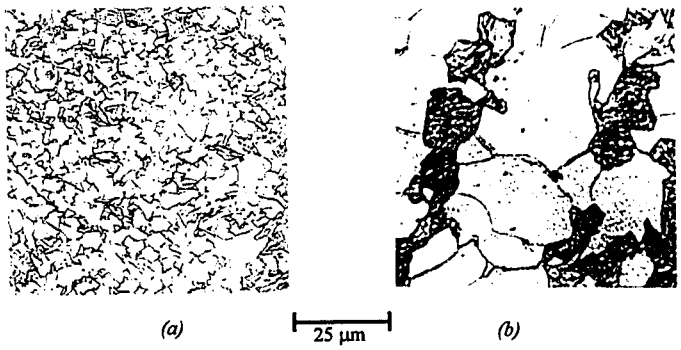

Fig. 4.6 (a) Recrystallized ferrite grains produced by straining to 0.8 at 3×10^{-4} s^{-1} at 800°C. (b) straining at 760°C, all else being equal, does not produce recrystallization.

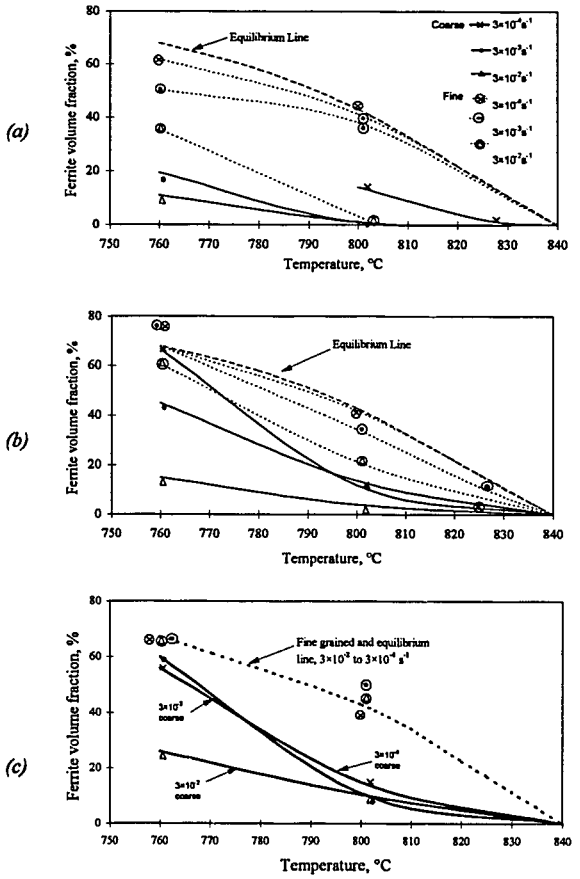

Fig. 4.7 *Effect of grain size, strain rate and temperature on the volume fraction of ferrite formed at strains of (a) 0.15, (b) 0.4 and (c) 0.8.*

From the graphs it can also be seen that reducing the grain size, in each case, significantly increases the amount of ferrite formed at a given temperature. The greatest difference between the coarse and fine grained samples appears at the lower strain rates (3×10^{-3} s^{-1} and 3×10^{-4} s^{-1}) and at the lowest strain (0.15). Under these conditions, one might expect grain size to be a particularly important factor as very little strain has been applied.

Increasing the strain rate, all other things being equal, was found to reduce the ferrite volume fraction; this effect can be attributed to the reduction in the time available for the transformation that accompanies an increase in strain rate. In the fine grained case, the effect of strain rate was most significant at the lowest strain for deformation at 800°C. However, one might hesitate to draw conclusions from this as it must be borne in mind that, at higher strains, equilibrium is being approached and therefore the reaction will inevitably slow, regardless of the effect of strain rate.

4.2.2.4 Influence of Strain on the Amount of Ferrite Formed During Compression

The dependence of ferrite volume fraction on applied strain for test temperatures of 800 and 760°C is shown in Fig. 4.8 (a) and (b), respectively. It can be seen from these graphs that, in the fine grained material, volume fractions moved very quickly towards equilibrium as the strain was increased. At the lower strain rates, equilibrium was reached in this material after less strain at 800 than at 760°C, a fact that can be attributed to some extent to greater straining of the parent material *before* the start of transformation at this lower level of undercooling. In the case of the highest strain rate, equilibrium volume fractions are reached more quickly at 760°C, which can be explained by considering the growing effect of time and the lessening effect of 'predeformation' of the austenite lattice as the amount of undercooling is increased.

In the coarse grained material at 800°C, little ferrite was formed beyond the thin films mentioned in section 4.2.2.1; the ferrite did not progress very far into the austenite matrix. At 760°C, volume fractions approaching equilibrium levels were only obtained at the lower strain rates. It is notable that, at higher strains at this temperature, ferrite was found to nucleate within the matrix, as well as at the grain boundaries.

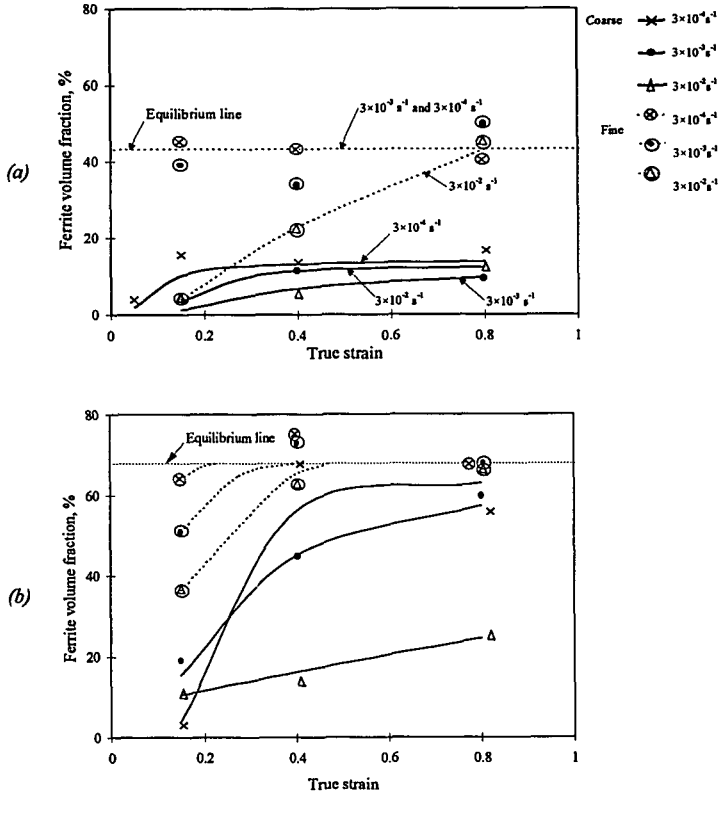

Fig. 4.8 *Dependence of ferrite volume fraction on strain at (a) 800°C and (b) 760°C in the fine and coarse grained materials.*

4.2.2.5 Influence of Time on the Amount of Ferrite Formed in both the Static and Dynamic Cases

By converting the relevant pairs of strains and strain rates into times, it is possible to plot the ferrite volume fraction found in the samples as a function of deformation time for the dynamic experiments. Such curves are plotted for test temperatures of 760 and 800°C in Figs 4.9 (a) and (b), respectively. The static data originally plotted in Fig. 4.1 are included in Fig. 4.9 (a) for comparison purposes. In order to identify trends in these graphs without making them unnecessarily complex, the data derived from the dynamic tests have been grouped according to prior austenite grain size, and the curves are drawn through these 'extended families' of points. As in the case of the static data, the curves are based on Avrami-type equations.

Returning to the figures, the first observation must be that there is significant scatter around the curves plotted through the enlarged data sets. This scatter is, as has been consistently the case in the present work, worse in the data derived from the fine grained samples. However, the fact that one can, with some courage, plot single lines through data sets linked only by prior austenite grain size suggests that the amount of strain and the rate at which it is applied are not the most critical factors. Rather it seems that, for a given temperature, prior austenite grain size, time, and whether or not the sample is being deformed are the more important parameters.

It should be noted that the four dynamic curves illustrated in Fig. 4.9 were obtained by essentially "averaging" the experimental points pertaining to three strain rates. It is nevertheless apparent that the approximated curves applicable to *individual* strain rates form families in which increasing the strain rate increases the kinetics of the transformation by about one order of magnitude. This effect can be compared with that of the application of concurrent straining, which leads to an average acceleration of 2 orders of magnitude in the coarse grained case and 2 ½ orders of magnitude in the fine grained case.

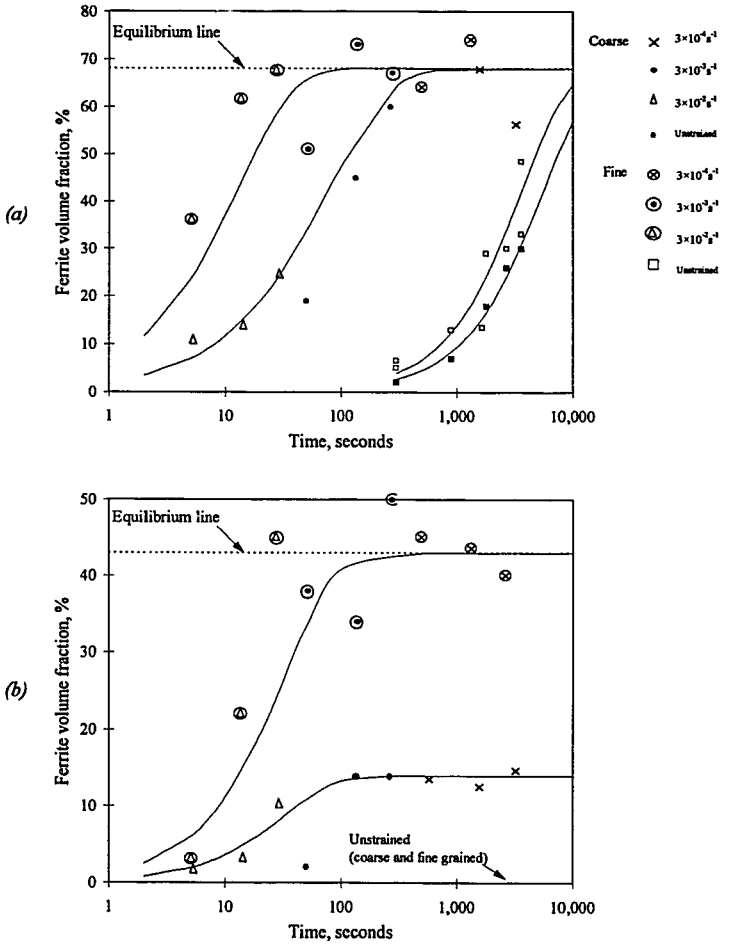

Fig. 4.9 *Influence of time on the formation of DIF in coarse and fine grained samples tested at (a) 760°C and (b) 800°C.*

Beginning with Fig. 4.9 (a), it can be seen that concurrent deformation has a very significant effect on the kinetics of the austenite-to-ferrite phase transformation at both the grain sizes examined—the curves are moved to shorter times by some two or more orders of magnitude. It is also evident from the curves that grain size has quite a significant effect on the rate of transformation during deformation. Equilibrium is reached after perhaps 100 s in the fine grained case, at which point the coarse grained material only displays around 60% of the equilibrium volume fraction.

At 800°C (Fig. 4.9 (b)), austenite grain size has an even more powerful effect on the transformation. After 100 s, ferrite formation in the coarse grained material was found to have slowed almost to a halt, with only 30% of the equilibrium amount present. In the fine grained material, on the other hand, at 500 s equilibrium was steadily being approached, and was reached in around 800 s. While the curve depicting the fine grained scenario resembles those shown in Fig. 4.9 (a), albeit moved to longer times (presumably due to a smaller driving force for the transformation), the curve plotted through the coarse grained datapoints is dramatically different. Initially rising as might be expected, it suddenly levels off, and remains almost flat over the range of times covered by these experiments. This phenomenon is considered in more detail in section 6.1.2.4.

4.2.2.6 Dynamic Transformation-Temperature-Time Diagrams

The results displayed in the previous section can be conveniently summarised on dynamic transformation-temperature-time (DTTT) diagrams. Such diagrams are presented in Fig. 4.10. For the fine grained, deformed case, lines are plotted for 5 (Fig. 4.10 (a)) and 95% (Fig. 4.10 (b)) transformed. However, because of the limitations imposed by the available data, this range could not be covered in the other cases. In the deformed, coarse grained material, and in both the undeformed scenarios, the upper limit is 30% transformed, as transformation was not observed to progress beyond this point during the current work in these cases.

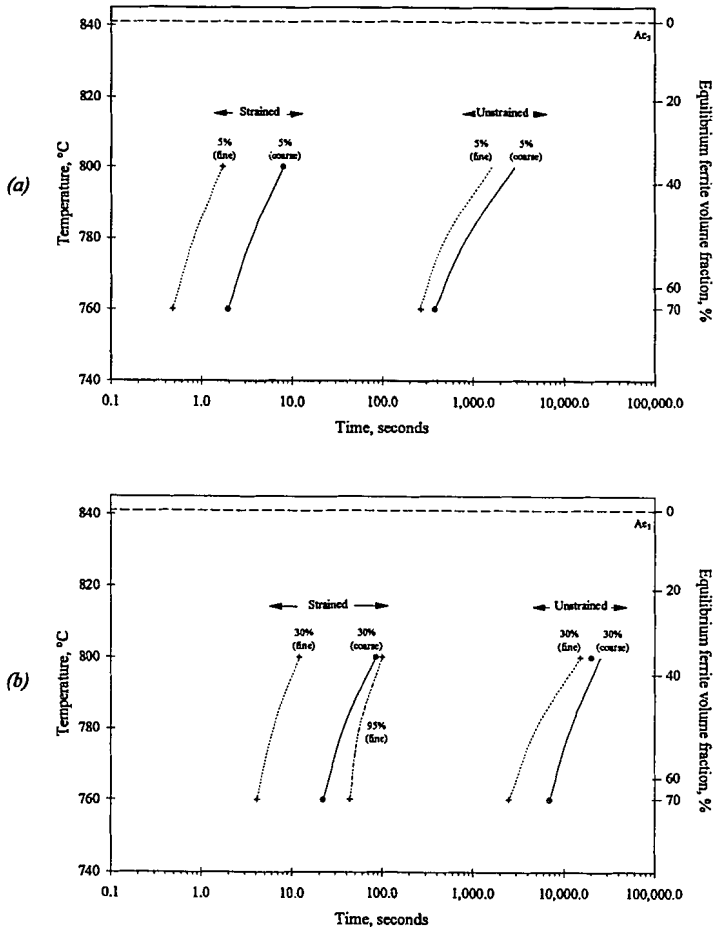

Fig. 4.10 Dynamic TTT diagrams for the formation of deformation induced ferrite from fine and coarse grained austenite.

While displaying much of the same information as was presented in Fig. 4.9, Fig. 4.10 demonstrates more emphatically the dramatic effect of deformation on the austenite-to-ferrite transformation. As stated in the previous section, deformation accelerates the transformation by about two and a half orders of magnitude. This is why DIF appears during the approximately 10 to 100 seconds available during straightening, while it is not at all possible for *static* ferrite to form (i.e. because the latter only appears after about 1000 s of holding at about 780°C). Grain size is also a significant factor in samples examined with and without deformation.

Chapter 5

Experimental Results Part 2:

The Effect of DIF on Hot Ductility

5.1 General Notes

The author would like to point out that, as described in Chapter 3, it was initially intended during the tensile part of this work to repeat all the thermal schedules that were examined as part of the compression testing phase. However, because of the suspect results obtained early in the tensile programme, changes were made to both the specimen dimensions and the testing set-up in order to reduce the thermal gradients found along the gauge lengths of the samples. Limitations regarding the amount of material available for re-machining meant that it would not be possible to repeat all of the thermal schedules used previously. It was therefore decided to concentrate on the coarse-grain thermal treatment (see section 3.3.3) as, based on the compression test results, this was by far the most likely to produce ductility problems.

5.2 Tensile Flow Curves

As with the compression test, the first piece of evidence gained from a tensile test is the flow curve; the curves obtained in the tensile part of the present work are plotted in Fig. 5.1. Referring to the figure, it is quite clear that there is a very significant effect both of strain rate and of test temperature on the shape of each of the plots. Increasing the strain rate increases the flow stress at all points of all the curves, as was the case with the compression specimens. The relative magnitude of this effect is consistent at all three temperatures examined.

The samples tested at 840°C (Fig. 5.1 (a)) provided plots that rise quite smoothly to a peak and then fall in a similarly even manner. Raising the strain rate at this temperature moved the point of fracture to larger strains, although it should be noted that after the onset of necking, the strain as measured by the LVDT (see section 3.2.4) is no longer true strain. Overall, the largest extensions to failure were recorded at this temperature.

The flow curves produced by the samples tested at 800°C (Fig. 5.1 (b)) are highly self-similar, as were those produced at 840°C, but are quite different from the curves produced at the higher temperature. There is a similar rise to a maximum, but the subsequent drop is very abrupt, the stress decreasing very quickly. At 800°C, increasing the strain rate moves the measured strain to fracture to greater values; this effect is far more significant at 800°C than the similar effect encountered at 840°C. It is notable that the peak stresses found at 800°C are not significantly greater than those achieved at 840°C—in fact the peak stress at the lowest strain rate at 800°C is slightly lower than that found at the higher temperature.

The curves produced at 760°C are once again self-consistent, but very distinct from those found at the higher temperatures. Each of these plots exhibits an extensive 'plateau', along which there is very little variation in flow stress. As with the curves generated at 800°C, the drop in flow stress leading to failure is abrupt. At this temperature, strain rate seems to have less of an effect on measured strain to failure—in this case the points of fracture are quite closely packed.

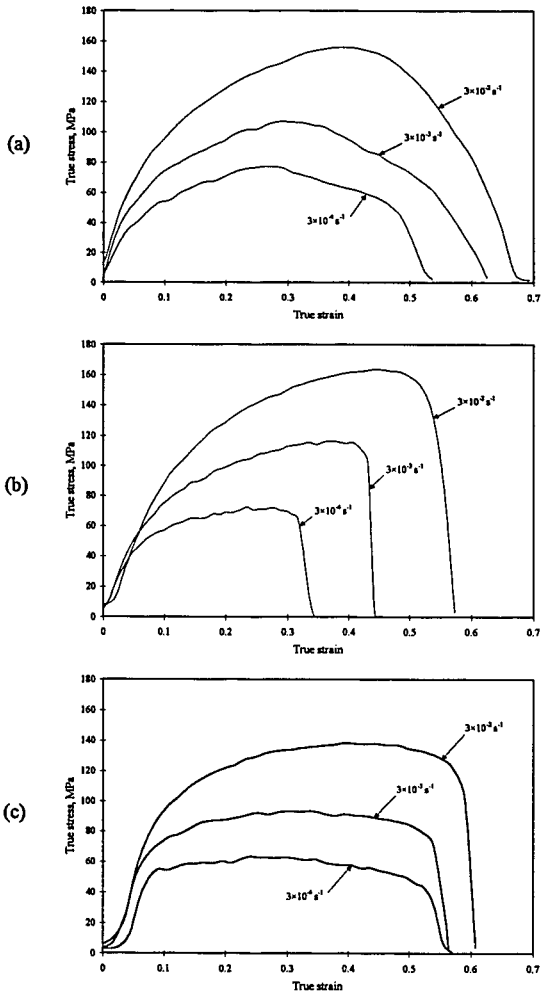

Fig. 5.1 *Tensile flow curves obtained at (a) 840, (b) 800 and (c) 760°C.*

5.3 Ductility Behaviour

As was explained in Chapter 3, in this work, percent reduction in area is taken to be a measure of tensile hot ductility. The three hot ductility curves obtained from the present tensile tests are plotted in Fig. 5.2.

Samples tested at 840°C at the two higher strain rates exhibited very good ductility, with reduction in area approaching 100%. At the lowest strain rate of 3×10^{-4} s^{-1}, however, relatively poor ductility was found. Decreasing the temperature to 800°C caused a marked decrease in ductility at all three strain rates. The largest drop occurred at the middle strain rate, a decrease of some 60%, while at a rate of 3×10^{-4} s^{-1}, the drop is some 20%. Decreasing the temperature further to 760°C resulted in an *improvement* in ductility in every case, although the values are still not up to the levels found at 840°C. At this lower temperature, the ductility levels found at each strain rate were quite similar.

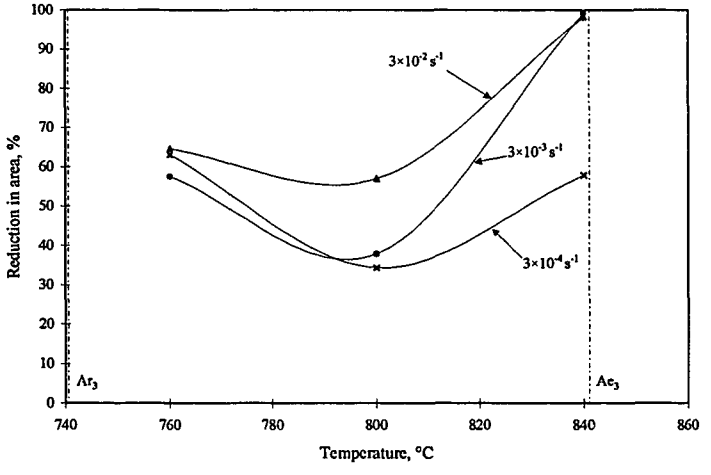

Fig. 5.2 Tensile hot ductility over the temperature range 760 to 840°C for the three strain rates examined.

Taken together, these curves show that the steel under investigation exhibits a ductility trough at all strain rates examined. The depth of this trough decreased as strain rate increased, while its width was impossible to determine from the present data as its lower limit appears to extend below the minimum temperature tested.

5.4 Metallographic Examination

5.4.1 General Observations

None of the samples tested at 840°C showed any measurable amount of ferrite upon microscopic examination—a purely martensitic structure was observed (see Fig. 5.3 (a)). Samples strained at 800°C, however, yielded measurable volume fractions, particularly at the lower strain rates (Fig. 5.3 (b)). At this temperature, nucleation was observed to occur mostly at the austenite grain boundaries, although some intragranular nucleation was also noted near the fracture surfaces. In cases where any significant amount of ferrite was present, failure was observed to occur in the bands of the second phase that had formed along the austenite grain boundaries. The thickness of the ferrite bands increased with decreasing strain rate, and therefore with increasing time at temperature. It was not obvious that any substructure had formed in the ferrite in the samples tested at this temperature.

Samples tested at 760°C were found to contain large quantities of ferrite: at the slowest strain rate, around 85% of the equilibrium volume fraction was present. The prior austenite grains appeared to be quite elongated along the tensile axis and were surrounded by thick bands of ferrite. At all strain rates, there appeared to be a large variation in ferrite grain size in the most heavily deformed areas near the fracture surface; this is apparently the result of partial recrystallization (Fig. 5.3 (c)).

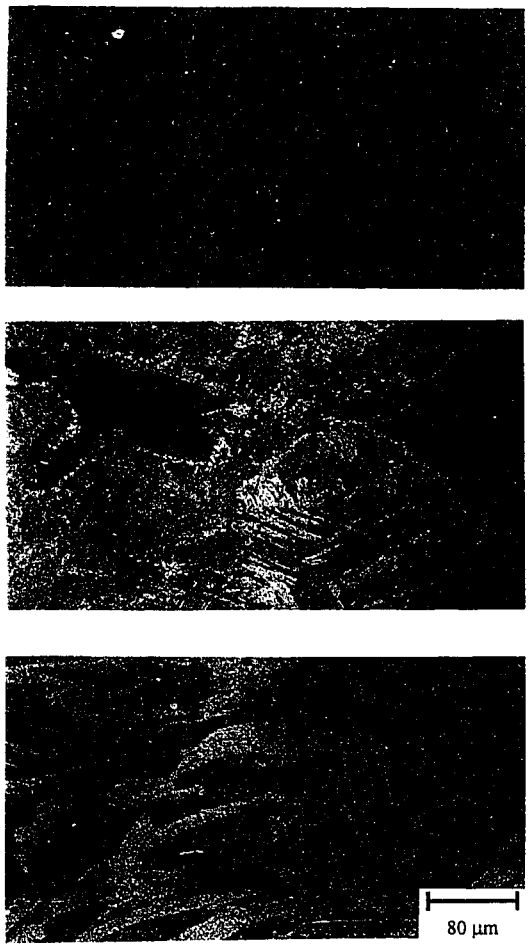

Fig. 5.3 *Examples of the microstructures found in the tensile samples. Tests performed at (a) 840°C, (b) 800°C and (c) 760°C at a strain rate of 3×10^{-3} s^{-1}.*

5.4.2 Effect of Tensile Test Parameters on Ferrite Volume Fraction

In the tensile portion of this work, the independent variables were test temperature and strain rate. The effect of strain rate on ferrite volume fraction over the temperature range examined is illustrated in Fig. 5.4. The curves depicted in the figure follow a form similar to that observed in the coarse-grained compression case (see Fig. 4.7), increasing in gradient as the temperature is decreased. Also similar to the compressive case is the fact that reducing the strain rate increases the volume fraction of ferrite formed: some 90% of the equilibrium value was found at 760°C at the slowest strain rate, where only 35% of that figure was produced at the highest strain rate. It should be borne in mind that, because of the strain inhomogeneities that are encountered in tensile tests, these figures cannot be compared directly with those obtained in compression.

It is also important to remember that, in the tensile case, one is not comparing like with like in terms of strain. For example, at 800°C, the measured strain to fracture (bearing in mind that this is not the uniform elongation) at a strain rate of 3×10^{-4} s^{-1} was

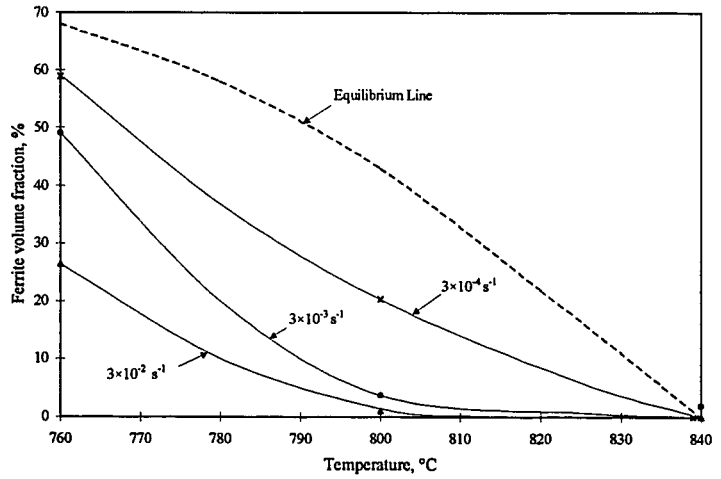

Fig. 5.4 Effect of strain rate and temperature on the ferrite volume fraction formed in tension.

around 0.35, whereas at 840 and 760°C it was more in the region of 0.55. This factor, and how it relates to the ductility of the sample in question, is considered further in the Discussion.

5.4.3 Fractography

The influence of the tensile test parameters on the ductility behaviour of the steel under examination was considered in Section 5.3. It is not surprising then that these parameters also have a significant effect on the fracture surface produced by testing to failure.

Fractographs of specimens tested at a strain rate of 3×10^{-3} s^{-1} at each of the three temperatures examined are presented in Fig. 5.5. The samples tested at 840°C all exhibited fracture surfaces similar to that shown in Fig. 5.5 (a), characterised by large voids (10-50 μm wide). Decreasing the strain rate increased the average size of the voids, such that at the slowest strain rate, they were in excess of 80 μm wide. This kind of fracture surface is indicative of a high temperature ductile rupture mode and is often found in the single-phase austenite region; it is normally associated with good ductility. The voids are thought to have developed from intergranular cracks which, as deformation proceeds, distort and elongate until failure occurs by necking between these already-separated areas. While the samples tested at the two highest strain rates did exhibit excellent ductility (see Fig. 5.2), the sample tested at 3×10^{-4} s^{-1} only produced a %RA value of some 60%, which cannot be considered to be particularly good. No qualitative difference beyond that already mentioned could be seen between the fracture surface obtained at 3×10^{-4} s^{-1}, and those found at the higher strain rates.

(a)

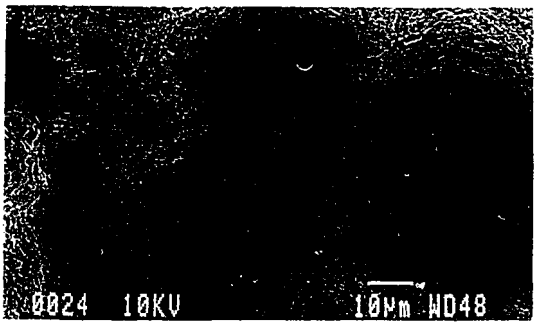

(b)

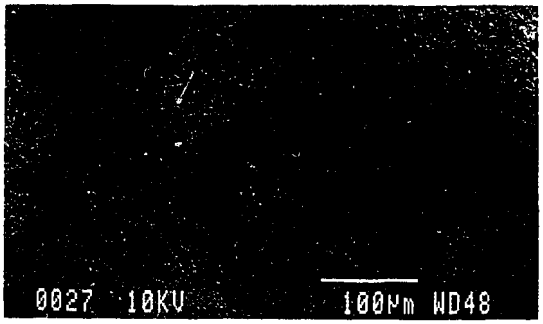

(c)

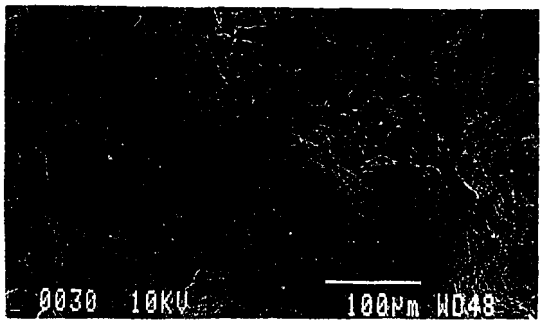

Fig. 5.5 *Examples of tensile fractographs. Samples tested at (a) 840, (b) 800 and (c) 760°C at a strain rate of 3×10^{-3} s^{-1}.*

All of the samples tested at 800°C exhibited relatively poor ductilities, ranging from 35 to 60 %RA. The largest reduction in area was exhibited by the sample tested at the highest strain rate; this sample contained less than 2% ferrite and yielded a fracture surface similar to those found at 840°C. The fracture surfaces of samples tested at the lower strain rates, however, appeared very different (Fig. 5.5 (b)). Measured amounts of ferrite were 4 and 21% for samples tested at 3×10^{-3} s^{-1} and 3×10^{-4} s^{-1}, respectively. In both cases, fracture appears to have been intergranular (i.e. between the *austenite* grains), with a large proportion of the final deformation going into the ferrite, which was shown in section 5.4.1 to have formed on the γ grain boundaries. Individual austenite grains are visible in the fractographs, covered in what appears to be heavily deformed ferrite. In these two cases, ductility was poor—between 35 and 40 %RA.

Samples deformed at 760°C all displayed improvements in ductility over those tested at 800°C. At this temperature, austenite grains became increasingly difficult to discern in the fractographs as the strain rate was decreased and the amount of ferrite formed increased. Even though at this temperature the strength differential between the austenite and the ferrite is decreased, fracture always occurred in the second, softer phase.

Chapter 6

Discussion

The Discussion chapter is split into three sections. The first deals with the formation of ferrite under undeformed as well as under compressive straining conditions. The second considers the effect of the austenite-to-ferrite transformation on the hot ductility of the steel in question. Finally, the third section presents a brief summary and assesses the industrial implications of the present work.

6.1 Ferrite Formation Under Static Transformation and Compressive Straining Conditions

Both in this and in previous studies,[65, 66] the deformation of unstable austenite has been shown to accelerate the γ-to-α transformation. Greater quantities of ferrite form under deformation than would form without strain, given the same incubation time and undercooling. Various mechanisms have been proposed to account for this, a number of which were described in section 2.4.2.1. The following discussion of the present results concentrates on the effect that prior austenite grain size, test temperature, and degree and speed of straining have on the amount, and on the morphology, of the ferrite formed upon the decomposition of thermodynamically unstable austenite. This section begins with

consideration of the static results, as these are the benchmark against which the remaining data will be compared.

6.1.1 Ferrite Formation Under Static Transformation Conditions

As was explained in section 3.3.3, the testing temperatures used in this work span a range from just below the Ae_3 to just above the Ar_3 temperatures of the experimental material. In this steel, this range is from 841 to around 740°C; most of the experiments were carried out at between 840 and 760°C. No ferrite was expected to be found in the samples tested under static conditions at 840°C—the equilibrium volume fraction predicted by the ThermoCalc software at this temperature was essentially zero (see section 3.3.3). At 800°C, however, the predicted equilibrium volume fraction was 43%, more than half that at 760°C (68%), and hence it is a little surprising that no ferrite was found in this case, given that at 760°C more than 50% of the equilibrium amount was present after 3,600 seconds of holding in the fine grained case (see Fig. 4.1).

The rate of ferrite formation at 760°C can be seen, in both the fine and coarse grained cases displayed in Fig. 4.1, to follow quite closely the 'S' curve normally adhered to by isothermal transformations in general. This is reassuring, as previous studies[86, 87] have shown that the particular case of isothermal transformation from γ-to-α can be described by the Avrami equation, which was used to plot these curves. Clearly ferrite forms faster in the fine grained case, and the curves suggest that equilibrium would be reached more quickly in this material, although it should be borne in mind that this second conclusion is based on nothing more than an extrapolation.

It is also quite clear from Fig. 4.1 that there is a significant amount more scatter in the fine grained case than there is in the coarse grained scenario, a fact that is consistently observed throughout the results, although one that seems to be more distinct in the unstrained samples. The most likely explanation for this enhanced variation is that there was a certain amount of macroscopic segregation left in the as-received source material, which was in the form of hot-rolled plate (see section 3.1). More direct evidence of this inhomogeneity may be found in Fig. 4.2 (c)—banding of the ferrite formed in the fine grained material is clearly visible, indicating that there are sizeable areas of the material

that are in some way predisposed to ferrite nucleation. One would expect the effect of such residual segregation to be greatest in the fine grained case as the heat treatment used to produce this type of material was based on an austenitizing temperature some 280°C lower than that employed for the coarse grained specimens (see section 3.3.3).

6.1.2 The Effect of Compressive Deformation on Ferrite Formation

6.1.2.1 Compressive Flow Curves

In section 4.2.1, it was noted that there is a significant effect of strain rate on the flow stress found at any point on the compressive flow curves. This effect is well established and is described by the Zener-Hollomon parameter, Z, which correlates directly with the resistance to plastic flow displayed by a metal during deformation. The Zener-Hollomon parameter can be thought of as a temperature-adjusted strain rate, and is given by:

$$Z = \dot{\varepsilon} \exp\left(\frac{Q}{RT}\right) \qquad \textit{Eq. 6.1}$$

where Q is an activation energy, $\dot{\varepsilon}$ the strain rate and T the absolute temperature. It can be seen from this equation that an *increase* in strain rate at constant temperature has the same effect (if not to the same degree) as a *decrease* in temperature at constant strain rate; i.e. they both cause an increase in flow stress. It should, however, be borne in mind that this relation, particularly as it relates to temperature, will not necessarily be followed in the dual-phase region. This is discussed in the section that follows.

6.1.2.2 Peak Stress Curves

The stress levels at the peaks that appeared in the compressive flow curves were found to vary with temperature, strain rate and prior austenite grain size. By reading the peak stress values from each of the flow curves and plotting the resulting figures against temperature, diagrams that display this variation can be produced. The curves obtained in this way for each austenite grain size and strain rate examined are presented in Fig. 6.1. Referring to the figure, one can see that from 1,000°C down to the Ae_3 temperature, the peak stress increases as the temperature is decreased in all cases, as expressed by the

Zener-Hollomon equation mentioned in the previous section. However, at the Ae_3 temperature, the curves begin to flatten out and at the lower strain rates, the strength actually falls with decreasing temperature. This change is abrupt at the lowest strain rate and is generally more pronounced at the finer austenite grain size.

The existence of stress maxima in the compressive flow curves can be accounted for using two different explanations: one that applies to phenomena encountered above the Ae_3, and a second that applies to mechanisms present below the Ae_3 temperature. In the former case, the peaks in the flow curves might be caused by the onset of dynamic recrystallisation in the austenite—the characteristic multi-peak behaviour was observed in the flow curves. In the latter case, the peaks found in the flow curves are related to the first detection of deformation induced ferrite in the microstructure.

Referring again to Fig. 6.1, it is notable that the fine grained case displayed lower peak strengths both above and below the Ae_3 for every strain rate examined. This is somewhat counter-intuitive since finer grains normally lead to a stronger aggregate. However, this phenomenon can be explained by considering the effect of grain size on

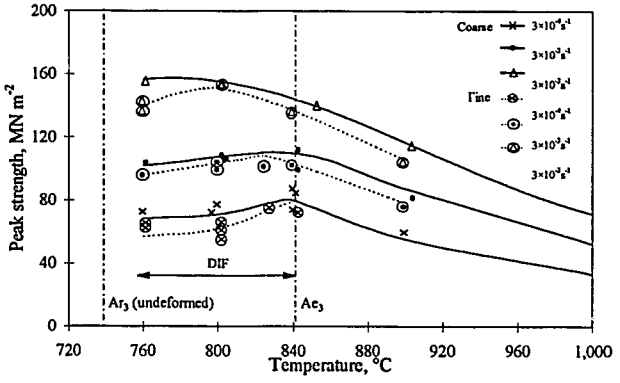

Fig. 6.1 Dependence of peak strength on test temperature in the coarse and fine grained materials at the three strain rates examined.

certain processes within the material. Above the Ae_3, finer grains reduce the critical strain for dynamic recrystallization, and thereby advance the point at which this softening process is initiated. Below the Ae_3, finer grains have been shown to accelerate ferrite formation,[82] which in turn reduces the flow stress of the mixture (see section 2.4.1). It is reassuring to note that, before the peak stress is reached, the flow stress for a given strain and strain rate in the austenite was in fact higher in the fine than in the coarse grained case, as would be expected for the entire test were it performed at room temperature. Fig. 6.2 compares flow curves in the coarse and fine grained cases for samples tested at 800°C at a strain rate of $3\times10^{-4}s^{-1}$.

6.1.2.3 Effect of Deformation on Ferrite Morphology and Distribution

The acceleration of ferrite formation by deformation seems to have a marked effect on the morphology, and on the distribution, of the resulting second phase. Maki et al.,[88] for example, showed that, under *static* transformation conditions, the ferrite morphology is particularly influenced by the austenite grain size. They found that relatively isolated, globular ferrite grains were formed in a C-Mn-Al steel with an austenite grain size of 100

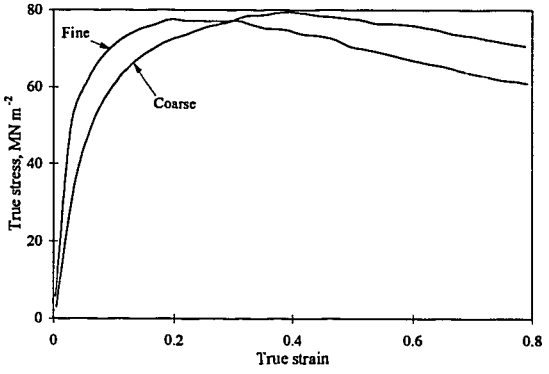

Fig. 6.2 Comparison of the flow curves obtained for fine and coarse grained samples tested at the same temperature and strain rate (800°C and $3\times10^{-4}s^{-1}$).

μm, whereas with a γ grain size of 350 μm, thin films of ferrite formed along the austenite grain boundaries. It appears likely that this difference is due to the fact that the ratio of triple point to grain boundary nucleation sites decreases with increasing grain size. Under *dynamic* conditions, however, these authors found that *deformation induced* ferrite always forms initially as thin films, regardless of the austenite grain size. Cardoso et al.[82] have also shown that thin films rather than more discrete ferrite colonies form in a Ti-containing steel with an austenite grain size of some 120 μm. The evidence provided by the above two sets of authors suggests that the effect of low strain rate deformation on the γ-to-α transformation is restricted to the neighbourhood of the grain boundaries. Growth of the ferrite away from the austenite grain boundaries seems severely restricted. A possible reason for this restriction is presented in section 6.1.2.4.

The trends in ferrite morphology noted above were closely followed in the present work. In the coarse grained material, ferrite formed as bands, decorating the austenite grain boundaries after comparatively small amounts of deformation (see Fig. 4.4). While decreasing the strain rate by two orders of magnitude (and therefore increasing the time spent under deformation by the same amount) slightly increased the widths of these films, the phase boundaries did not move significantly towards the centres of the austenite grains until the test temperature was lowered to some 100°C below the equilibrium transformation temperature.

In the fine grained material, transformation progressed more quickly in all cases. The largest difference in transformation rate between the coarse and fine grained samples appeared at the higher temperatures examined. The DIF formed in the fine grained specimens, while not like that formed under static conditions, was more blocky in appearance than that formed in the coarse grained material. However, the comparison of Table 4.1 with Table 4.2 reveals that the ferrite grains formed in the fine grained samples progressed no further into the austenite matrix than the 'films' formed in the coarse grained material.

6.1.2.4 Effect of Time Under Deformation on the Amount of DIF Formed

Some of the most striking results from the compression testing phase of this work were discovered upon plotting the amount of ferrite formed against the time spent under deformation. The resulting curves were plotted in Fig. 4.9.

Beginning with Fig. 4.9 (a), it can be seen that, at 760°C, the effect of increasing the grain size is as one might initially expect—to retard transformation; in this case the curve is moved to increased times by approaching one order of magnitude. However, moving to Fig. 4.9 (b), which depicts the situation at 800°C, the effect of increasing grain size is far more dramatic, and plainly quite different than that encountered at the lower temperature. In the case of this second graph, the line traced through the points plotted from the coarse grained material appears almost to level off at around 14% ferrite, some 1/3 of the equilibrium fraction, and shows little sign of moving any further towards the stable amount. The abrupt levelling of this curve suggests that some barrier to further ferrite formation has been reached; if this is the case, then, judging by the curve, the fine grained material does not meet with such an obstacle.

A possible explanation for this phenomenon can be arrived at by combining observations from the present work with information drawn from the literature. Before beginning to explain this mechanism, a few facts noted elsewhere in this thesis are worthy of reiteration:

1. Given that this sudden stalling of the γ-to-α transformation was encountered during deformation, and that no such phenomenon has been reported in static cases in the literature, it must be assumed that the reason for this effect is some corollary of the deformation process.
2. As was mentioned in section 2.4.1, the plastic deformation of a metallic polycrystal is not homogeneous. When austenite is deformed at low strain rates, much of the strain is taken up by grain boundary sliding and by slip in regions close to the grain boundaries.
3. As a result of the above point, a high dislocation density is present in the vicinity of the grain boundaries, which the γ is slow to remove as its low

SFE makes recovery difficult. (It is further notable that two of the publications that attempt to account for the effect of deformation on the γ-to-α transformation, as described in section 2.4.2.1,[66, 68] cite the ferrite nucleation occurring in heavily deformed parts of the austenite matrix, which are located near to the grain boundaries.)

The present work suggests that, when the undercooling is relatively small, ferrite forms quickly in the deformed regions near the grain boundaries, but is unable to 'escape' this region. This is visible only in the coarse grained case in the present work because deformation becomes less confined to the grain boundaries as the grain size is decreased. McLean[89] produced the schematic diagram shown in Fig. 6.3 based on hardness measurements in cold-worked polycrystals. This shows that, with fine grains, the deformation is quite homogenous, progressing right into the interiors of the grains. With a sufficiently large grain size, on the other hand, the interior of a grain may almost completely escape the restraints, and accompanying heavy deformation, imposed by the grain boundaries. This results in a highly heterogeneous structure, and produces a smaller overall increase in dislocation density.

With the idea of strain inhomogeneity established, the question then becomes, how wide is this deformation zone in a relatively coarse-grained aggregate? A ball-park figure

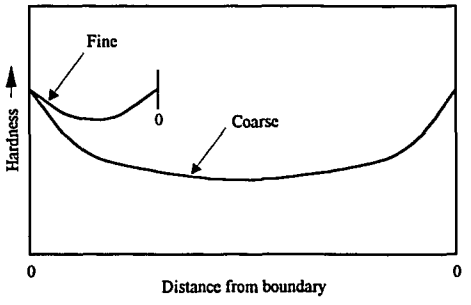

Fig. 6.3 Effect of grain size on the local hardness of individual grains.[89]

may be obtained from the work of Bay and Hansen,[90] who found bands of subgrains between 2 and 8 μm wide in 99.4% pure aluminum polycrystals, strained to 0.36 by cold rolling, with a grain size of 370 μm. While the point that these authors make is one of enhanced recovery in the grain boundary region due to heavy deformation in its vicinity, the width of heavy deformation could be applicable to the present work.

The strain applied in the aforementioned work is almost exactly in the middle of the range imposed in the present experiments, although the grain size used was some 85% larger than that employed here (200 μm in the coarse grained case). Nevertheless, if one assumes that the heavily deformed regions formed in the coarse grained samples in the present case were the same proportion of the mean grain diameter as those found in Bay and Hansen's work, then one obtains a maximum band width of 4.3 μm. Now, the equilibrium ferrite volume fraction at 800°C is 43%; assuming that nucleation does not occur in the centres of the grains (which has been shown largely to be the case under the conditions imposed here), ferrite must progress some distance into the austenite grains in order to attain this stable level. Adopting a simple model of a spherical austenite grain, as sketched in Fig. 6.4, the ferrite must progress into the austenite matrix to a distance $r_1 - r_2$, where these are the radii of the austenite grain before and after formation of the equilibrium volume fraction of ferrite.

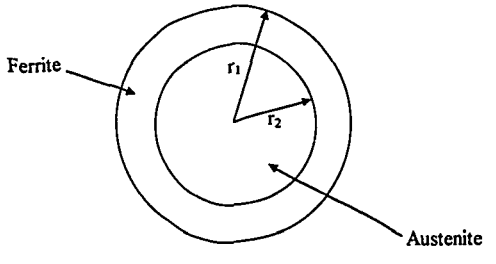

Fig. 6.4 *Simple model of a spherical austenite grain, surrounded by a uniform band of ferrite.*

Taking the austenite grain sizes to be 200 and 25 μm in the coarse and fine grained cases, respectively, and the equilibrium ferrite volume fraction to be the calculated value of 43% at 800°C, one finds that the ferrite must progress ~17 μm in the coarse, and 2 μm in the fine grained case, in order to achieve equilibrium. Working in the opposite direction, taking the 4.3 μm deformed band width estimated earlier, one finds that this corresponds to a transformation of 10% in the coarse grained case, a figure which is comparable with the 14% level at which the transformation stalled in the present experiments.

In the fine grained case, the model predicts that equilibrium can be reached after very little progression of the ferrite into the austenite matrix. However, in this case, the distance required may not be important as the deformation is much more homogeneous, and there is not as significant a "deformation gradient".

It must, of course, be remembered that this is a very simple model, and that the figures used may or may not be directly applicable to the system in question. However, it is of interest to note that the estimates obtained agree closely with the observations, and indicate that the proposed explanation is reasonable. Of course, more experiments would be required were this to be confirmed.

6.1.2.5 Effect of Strain Rate on the Amount of DIF Formed

There may also be some relationship between strain rate and the degree to which the ferrite manages to progress into the γ matrix. Previous work[27, 34] has demonstrated that there is less progression of the ferrite into the austenite matrix when the strain rate is low (e.g. around 3×10^{-4} s^{-1}). At this strain rate, it was suggested, almost full recovery can take place in the α. This means that, even after appreciable deformation, there remains a significant difference between the strength of the γ matrix and that of the ferrite formed on its boundaries. The ferrite makes greater advances into the austenite matrix when the strain rate is higher as work hardening of the ferrite reduces the strength difference between these phases.

Unfortunately, in the present work, this effect could not be assessed because of the fact that the strain rates were varied over three orders of magnitude while the amount of

deformation, owing to the nature of the compression test, was only varied by *approaching* one order of magnitude. The result is that no two tests can be compared directly in terms of time; therefore the effect of the *rate* at which deformation is applied to the material over a fixed period of time cannot be determined with any confidence.

6.2 Hot Ductility in the Dual-phase Region

6.2.1 Analysis of the Tensile Flow Curves

As is often the case with tensile data, the flow curves produced in this part of the present work can each be divided into three distinct sections: the linear or elastic region, the region of uniform elongation, and the region of stress and strain localisation. As was noted in section 5.2, the tensile flow curves obtained at a given temperature were highly self-similar, so in order to facilitate comparison of the curves found in each case, the flow curves obtained at the middle strain rate (3×10^{-3} s^{-1}) at each of the three temperatures examined are collected and displayed in Fig. 6.5.

6.2.1.1 Elastic/Initial Plastic Deformation

In the first part of the stress/strain curves, the stress rises comparatively rapidly, and in a relatively continuous fashion, as the strain is applied at all the temperatures and strain rates examined. This region is at least partly elastic, although in this work its upper limit is impossible to define as no yield point is observed—there is merely a gradual decrease in the gradient of the curve.

At 840 and 800°C, i.e. the two higher temperatures tested, the gradient of the flow curve at any point in the elastic/initial plastic zone decreases with strain rate (Fig. 5.1). This effect appears most pronounced at the lower of these two temperatures, but is practically absent in the specimens tested at 760°C; in this case the gradients of the three curves are practically identical. The steepest gradients were found at 760°C, while the curves obtained at this temperature also show the most abrupt change in gradient as softening processes are suddenly activated.

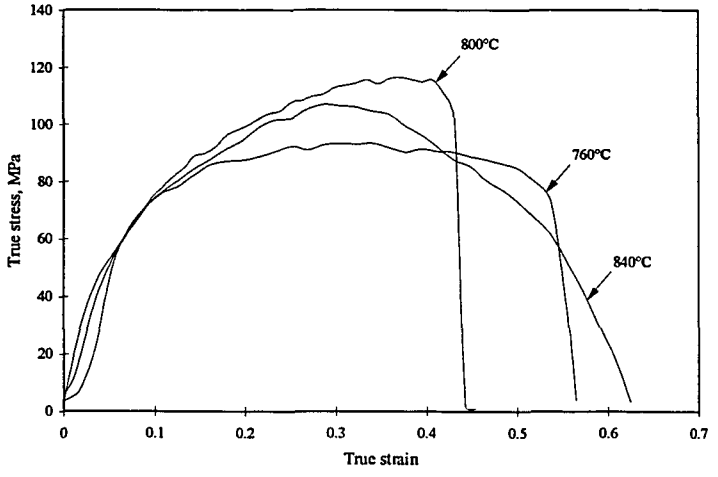

Fig. 6.5 Comparison of tensile flow curves observed at different temperatures.

6.2.1.2 Uniform Elongation

The second stage of deformation is that in which uniform elongation occurs. Before proceeding with this section, it is worth noting that the apparent waviness found in these portions of certain of the curves obtained in this work is likely not a material trait, but is due to scatter in the readings taken by the computer from the LVDT during the experiment. Plotting crude curves through these slightly scattered points leads to the undulations. There are two major factors responsible for producing the variation in the data: first, electrical interference between the high voltage, high current, furnace power supply and the LVDT; second, the fact that the test proceeds in incremental steps, as defined by the testing program. Referring to Fig. 5.1, it can be seen that the variation is at a minimum at the highest strain rate, where the step rate was inevitably the greatest. Measures undertaken to minimize these sources of error were (a) the definition of a large number of steps for each deformation routine, and (b) the movement of the furnace power supply cable as far away from the LVDT as possible.

Returning to a description of the curves, if the material were, in the single-phase region at least, to correlate well with the Zener-Hollomon parameter, then the gradient of the uniform elongation portion of the tensile flow curve should be dependent on both the strain rate and the test temperature. Temperature, of course, is one factor that controls the rate at which softening processes can remove the work hardening that is constantly accumulating in the material. From Fig. 5.1, it can be seen that in each of these experiments, the stress increases to a maximum as the strain is applied and the material work hardens. At all of the three temperatures, an increase in strain rate brings about an increase in the gradient of this portion of the curve, as per the theory. However, decreasing the temperature from 840 to 800°C does not substantially increase the gradient of the curve at a given point in this region; rather, for a given strain rate, they remain similar, as illustrated in Fig. 6.5. Decreasing the temperature further to 760°C prompts a reduction in the gradient of the uniform elongation portion of the curves, and a significant reduction in the peak true stress applied to the material.

6.2.1.3 Strain Localisation

Necking begins when, macroscopically, the increase in stress due to a decrease in the cross-sectional area of some part of the specimen exceeds the increase in strength in that area that occurs simultaneously due to work hardening. It can be shown that at the point of tensile instability,

$$\frac{d\sigma}{d\varepsilon} = \sigma \qquad \textit{Eq. 6.2}$$

where σ and ε are true stress and true strain, respectively. This is known as the Considère criterion.[91] In a simple, room temperature tensile test, necking is initiated at the maximum load; this is also the case in experiments conducted at high homologous temperature. However, in these cases, the loss in work hardening ability is often accompanied by the action of various softening mechanisms. One 'softening mechanism' that was encountered in this work was the formation of deformation induced ferrite.

In the present case, because of the 'waviness' of the stress-strain curves, it was rather difficult to determine the precise point at which strain localisation began.

Nevertheless, in certain cases, the strain at the onset of necking was estimated by assuming that the diameter outside the necked region corresponded to the diameter at the onset of plastic instability. However, this approach could not be applied to the specimens displaying relatively good ductilities, for which the necked region extended along the entire gauge length. As a result of this uncertainty, no attempt will be made to suggest precisely the strain at which necking first began in the samples tested during this investigation; instead, it is the point at which the stress began to decrease that will be highlighted.

At 840 and 800°C, the point at which necking is initiated is dependent on strain rate. At both temperatures, decreasing the strain rate advances the strain at which flow localisation occurs—the largest dependence is at 800°C, at which temperature the sample tested at 3×10^{-2} s^{-1} only began to neck after almost double the strain of that tested at 3×10^{-4} s^{-1}. At 760°C, however, necking occurred at similar strains for all three strain rates.

The behaviour during necking is clearly very dependent on test temperature, although it is not so clearly affected by strain rate. At 840°C, the stress drops off relatively gradually, fracture occurring after a considerable amount of more straining has occurred. At 800 and 760°C, however, fracture occurs very rapidly after necking begins—little additional plastic deformation occurs. This is particularly the case at 800°C.

6.2.2 Analysis of the Hot Ductility Curves

The hot ductility curves presented in section 5.3 show that a ductility trough is encountered in the steel in question at all the strain rates examined. The minimum ductility appears to occur at around 800°C. The curves, displayed in Fig. 5.2, increase in depth as the strain rate is lowered, and therefore follow trends found in other work, although this effect does not appear as marked as that previously found in higher carbon grades.[34] As was also noted in section 5.3, the widths of the troughs found in the present work are impossible to assess as the zone of poor ductility appears to extend beyond the lowest temperature tested here. This is not entirely surprising, as it has been reported in the past[21] that the ductility trough encountered in plain carbon steels normally extends to some temperature below the static Ar_3 temperature. The recovery in ductility in this case would therefore have been out of the range of the current experiments.

Comparing the tensile flow curves presented in Fig. 5.1 with the ductility curves shown in Fig. 5.2 and the micrographs and fractographs displayed in Figs 5.3 and 5.5, respectively, it becomes increasingly apparent that there is a very close link between ductility, flow curve shape, and microstructure. As was mentioned above, the minimum ductility was displayed at 800°C, at which point the tensile flow curves show abrupt strain localisation and maximum sensitivity of elongation to fracture to strain rate. This temperature also gave the lowest overall extension to failure.

Given the rates of deformation applied, the temperatures used (i.e. between the Ae_3 and undeformed Ar_3), and nature of the experimental material (i.e. the absence of microalloying elements), the most likely reason for the ductility troughs is the formation of deformation induced ferrite. This was demonstrated in section 5.4, where fracture was shown to occur along the thin films of ferrite formed at the austenite grain boundaries. It is notable that, even when 60% ferrite is present in the microstructure, which should be enough to prevent strain concentration (see section 2.4.1), the flow curves show the same abrupt downturn upon necking. The effect of the additional ferrite is to increase the length of the stress 'plateau' noted in these curves, and to reduce the dependence of the elongation to failure on the strain rate. As the onset of plastic instability is controlled by the ability of the material in question to work harden (see section 6.2.1.3), it seems likely that the sudden occurrence of necking observed when ferrite is present is due to the rapid recovery that occurs in this phase.

When the ductility trough in steel is caused by ferrite formation at austenite grain boundaries, it is generally accepted that the ductility recovers when either the ferrite is removed, or, as has been indicated above, when there is a large enough quantity of it present to prevent significant strain concentrations from occurring. It is interesting then to plot ductility (as measured by %RA) against ferrite volume fraction for each of the tensile tests performed in the present work; here the aim is to determine the quantities of ferrite associated with poor ductility. This is done in Fig. 6.5.

It can be seen from the figure that all (apart from one) of the points fall on the kind of curve that is expected from the above discussion. Where no ferrite is present, the

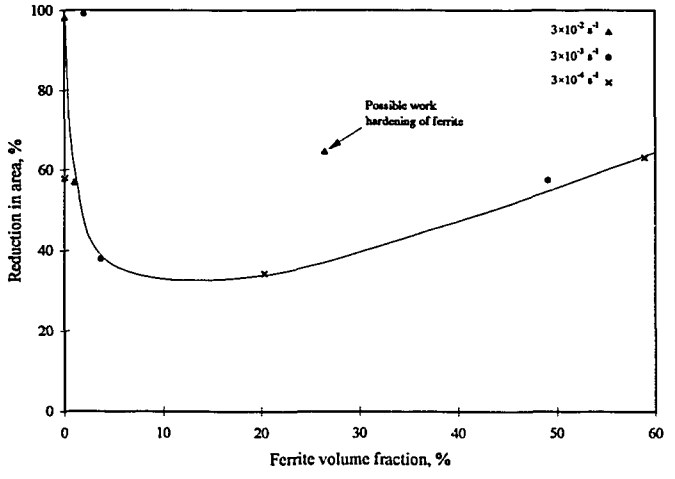

Fig. 6.6 Effect of ferrite volume fraction on tensile hot ductility.

ductility is excellent, with the reduction in area approaching 100%. However, as small amounts of ferrite are formed on the grain boundaries, the ductility drops dramatically and only recovers when quite significant amounts of this second phase are present.

The point that does not fit the curve is from a test conducted at 760°C (the lowest temperature examined), and at the highest strain rate. Two factors are therefore worthy of note. Firstly, as the temperature is reduced, so the difference between the strengths of the γ and α is decreased. Secondly, increasing the strain rate, of course, makes it more difficult for recovery to remove work hardening in the time available. It must be remembered, of course, that this is the result of only one test, and so should not be taken as definitive. However, it might be argued that the above two factors, when combined, conspire to reduce the strength differential between austenite and ferrite sufficiently to partially abate the effects of strain concentration in the softer phase. The result is surprisingly good ductility.

6.3 Summary and Industrial Implications

This work adds to the already considerable body of knowledge that has grown up around the problem of transverse cracking. It concentrates on the ductility trough found in most coarse grained plain carbon steels in the vicinity of the two-phase region, and sets out to assess the effect of the austenite-to-ferrite transformation on the tensile hot ductility.

The main point that has been arrived at through this work is that, at low strain rates and small applied strains, increasing strain rate *decreases* the amount of ferrite present in the microstructure because it *decreases* the amount of time available for ferrite formation. Time seems particularly important as, in coarse grained steels, the formation of *deformation induced* ferrite has been found to be limited to regions *significantly* affected by deformation. At the slow strain rates involved in the unbending operation, this means narrow bands adjacent to the grain boundaries. The limited width of these deformed regions makes the formation of enough ferrite to improve the ductility sufficiently unlikely to be achieved at low levels of undercooling.

From an industrial point of view, the results of the present work suggest that, in the continuous casting of plain carbon steels, unbending at a high temperature and at as high a strain rate as possible should reduce the incidence of transverse cracking. Of course, there are many factors that influence unbending temperature and casting speed, and each must be weighed on its merits. Happily though, these ideas of maximising the unbending temperature (and to a lesser extent, increasing the casting speed) tally well with modern ideas with regard to hot charging and direct rolling, where the bottleneck is the continuous caster.

Chapter 7

Conclusions

The effects of strain, strain rate, undercooling and grain size on the austenite-to-ferrite transformation have been investigated, and the results applied to the assessment of the hot ductility of the steel in question. The following conclusions can be drawn from this work:

1. Deformation induced ferrite forms in both fine and coarse grained steels at temperatures only a few degrees below the Ae_3. The present work indicates that, particularly at low levels of undercooling, the rate of ferrite formation when deformation is being applied is several orders of magnitude greater than in the absence of straining.

2. At relatively modest undercooling (~40°C), deformation induced ferrite seems not to form outside regions of the material that are *directly* affected by the applied strain. At the low strain rates imposed here, this means that, in coarse grained materials (~200 μm), deformation induced ferrite only forms in narrow bands, adjacent to the grain boundaries. In fine grained materials (~25 μm), deformation is far more homogeneous, and therefore ferrite formation is not so severely limited or localized.

3. The tensile hot ductility, in the intercritical or dual-phase region, of the steel used in the present work is clearly linked to the austenite-to-ferrite transformation. When narrow bands of ferrite form at the austenite grain boundaries, failure always occurs in this second phase. Ductility is at a minimum when around 10% ferrite is present, and only begins to recover substantially when more than ~50% ferrite has formed in the microstructure.

4. Given that unbending involves small strains (≈ 3%) applied at a low strain rate ($\sim 3\times10^{-4}$ s^{-1}), it is unlikely that sufficient ferrite can to form during the 100 s that are available to provide good ductility during this operation. This conclusion is based on the assumption that the present experiments simulate reasonably faithfully the industrial conditions of interest.

5. From an industrial perspective, unless unbending can be performed at strain rates in excess of 3×10^{-2} s^{-1}, this operation must be carried out above the Ae_3 or below the (undeformed) Ar_3 temperature if transverse cracking is to be prevented.

References

1. H. Bessemer, J. Iron and Steel Inst., 3 (1891), 23.
2. R. M. Daelen, German Patent No. 51217 (30 July,1889).
3. S. Junghans, US Patent No. 2135, (1 November, 1938).
4. International Iron and Steel Inst., Annual Statistics (1991).
5. P. Nilles and A. Etienne, "Continuous casting: status and prospects", 1st European Conference on Continuous Casting, Florence, Italy (1991).
6. W.R. Irving, "Continuous Casting of Steel", The Institute of Materials, London (1993).
7. International Iron and Steel Inst., "A study of the continuous casting of steel", Brussels (1977).
8. F. K. Iverson and P. Kappes, "Innovative minimill concept for flat production at Nucor's new Crawfordsville, Indiana, plant", 4th International Conference on Continuous Casting, Brussels (1988), 767.
9. A. L. Robson and G. L. Thompson, Materials World, 3, No. 5 (1995), 222.
10. L. L. Teoh, J. Mater. Proc. Technol., 44 (1994), 249.
11. T. Fastner, H. Nartz, J. Vlcek, W. Marschal, H. Preissl, and N. Hubner, Metall. Plant and Technol. Int., 18, 2 (1995), 6.
12. H. F. Shrewe, "Continuous Casting of Steel", Verlag Stahleisen mbH, Dusseldorf (1987).
13. K. Yoshida, T. Kobayaski, M. Tanaka and T. Watanabe, 4th International Iron and Steel Congress, The Metals Society, London (1982), Paper 4.

14. J. K. Brimacombe and K. Sorimachi, Metall. Trans. B (1977), 489.

15. A. Etienne and W. Irving, Proc. 1985 International Conference on Continuous Casting, "Continuous Casting '85", The Institute of Metals, London, England (1985), 11.

16. International Iron and Steel Inst., Continuous casting of steel 1985—A Second Study (1985).

17. J. K. Brimacombe and I. V. Samarasekera, "Fundamental Analysis of the Continuous Casting Process", In: Thermomechanical Processing of Steel, Centre for Metall. Process Engineering, Univ. of British Columbia, Vancouver BC (1989), 1.

18. W. J. Lankford, Metall. Trans., 3 (1972), 1333.

19. J. M. Arrowsmith, 'Steel Research 1977', BSC, London, 13 (1978).

20. H. Von Ende and G. Vogt, J. Iron Steel Inst., 210 (1972), 889.

21. B. Mintz, S. Yue and J. J. Jonas, Int. Mater. Rev., 36, No. 5 (1991), 187.

22. Y. Maehara, K. Yasumoto, Y. Sugitani, and K. Gunji, Trans. Iron Steel Inst. Jpn., 25 (1985), 1045.

23. A. Vaterhaus, Trans. Iron Steel Inst. Jpn., 23, 7 (1983), B-242.

24. J. Y. Fu, C. I. Garcia, S. Pytel, and A. J. De Ardo, 'Processing, Microstructure and Properties of HSLA Steels", Metallurgical Society of AIME, Warrendale, PA, (1988), 27.

25. P. Deprez, J. P. Bricout and J. Oudin, J. Mater. Proc. Technol., 32 (1992), 325.

26. B. Mintz and R. Abushosha, Mater. Sci. Technol., 8 (1992), 171.

27. B. Mintz and J. J. Jonas, Mater. Sci. Technol., 10 (1994), 721.

28. C. Ouchi and K. Matsumoto, Trans. Iron Steel Inst. Jpn., 22 (1982), 181.

29. H. C. Chang and N.J. Grant, Trans. AIME, 206 (1956), 544.

30. B. Mintz, J. R. Wilcox, and D. N. Crowther, Mater. Sci. Technol., 2 (1986), 589.

31. Y. Meahara and Y. Ohmori, Mater. Sci. Eng., 62 (1984), 109.

32. P. J. Wray, Met. Technol., 12 (1981), 466.

33. D. N. Crowther and B. Mintz, Mater. Sci. Technol., 2 (1986), 671.

34. B. Mintz, R. Abu-shosha and M. Shaker, Mater. Sci. Technol., 9 (1993), 907.

35. N. J. Grant and A. W. Mullendore, "Deformation and Fracture at Elevated Temperatures", MIT Press, Cambridge, MA, USA (1965).

36. J. R. Wilcox and R. W. K. Honeycombe, Met. Technol., 11 (1984), 217.

37. D. N. Crowther, Z. Mohammed, and B. Mintz, Trans. Iron Steel Inst. Jpn., 27 (1987), 366.

38. B. Mintz, R. Abushosha and J. J. Jonas, Trans. Iron Steel Inst. Jpn., 2, 32 (1992), 241.

39. H. G. Suzuki, S. Nishimura, J. Imamura and Y. Nakamura, Trans. Iron and Steel Inst. Jpn., 24 (1984), 169.

40. K. Yasumoto, Y. Maehara, S. Ura and Y. Ohmori, Mater. Sci. Technol., 1 (1985), 111.

41. T. Sakai and M. Ohashi, in "Physical Metallurgy of Thermomechanical Processing of Steels and Other Metals, Thermec '88", The Iron and Steel Institute of Japan (1988), 162.

42. B. Mintz, S. Yue and J. J. Jonas, in Proc. Int. Conf. On "Recrystallization in Metallic Materials", Wollongong, NSW; Metallurgical Society of AIME (1990), 553.

43. G. I. S. L. Cardoso and S. Yue, "31st Mechanical Working and Steel Processing Conference", Iron and Steel Society of AIME, Chicago (1989), 585.

44. G. I. S. L. Cardoso, M. Eng. Thesis, McGill University, Montreal, Canada, 1990.

45. R. W. K. Honeycombe, "Steels: Microstructure and Properties", Halstead Press, New York (1995).

46. D. A. Porter and K. E. Easterling, "Phase Transformations in Metals and Alloys", Second Edition, Chapman and Hall, London (1992).

47. W. D. Callister, Jr., "Materials Science and Engineering: An Introduction", Third Edition, John Wiley and Sons, New York (1994).

48. J. W. Christian, "The Theory of Transformations in Metals and Alloys", Second Edition, Pergamon Press, Oxford (1975).

49. P. J. Clemm and J. C. Fisher, Acta Met., 3 (1955), 70.

50. "Atlas of Isothermal Transformation and Cooling Transformation Diagrams", American Society for Metals, Metals Park, OH, USA (1977).

51. H. I. Aaronson, "Decomposition of Austenite by Diffusional Processes", Interscience, New York (1962), 387.

52. H. I. Aaronson, C. Laird and K. K. Kinsman, "Phase Transformations", American Society for Metals, Metals Park, Ohio, USA (1970).

53. A. K. Sinha; 'Ferrous Physical Metallurgy", Butterworths, Boston (1989).

54. Metals Handbook, Vol. 9, "Metallography and Microstructures", 9th Edition, ASM International, Metals Park, OH, USA (circa 1980).

55. R. D. Doherty, Metal Science, 8 (1974), 132.

56. M. Umemoto and I. Tamura, Proc. Conf. HSLA Steels '85, CSM, Beijing, China, (1985), 373.

57. R. W. K. Honeycombe, "The Plastic Deformation of Metals", Second Edition, Edward Arnold, London (1984).

58. H. J. McQueen and J. J. Jonas, "Plastic Deformation of Metals", Treatise on Materials Science and Technology, 6, Academic Press, New York (1975).

59. V. M. Urie and H. L. Wain, J. Inst. Met., 81 (1952), 153.

60. D. McLean, J. Inst. Met., 81 (1952), 293.

61. E. A. Simielli, Ph.D. Thesis, McGill University, Montreal (1990).

62. R. W. K. Honeycombe and W. Boas, Aust. J. Scient. Res., 1 (1948), 70. Cited in reference 57.

63. L. M. Clarebrough, Aust. J. Scient. Res., 3, (1950), 72. Cited in reference 57.

64. F. E. Al-Jouni and C. M. Sellars, "Deformation of Multi-Phase and Particle Containing Materials", Ed. J. B. Bilde-Sorenson, Risø Natl. Lab., Roskilde, Denmark (1983), 131.

65. M. Umemoto, H. Ohtsuka, H. Kato and I. Tamura, Proc. Int. Conf. on Structure and Properties of HSLA Steels, Wollongong, Australia (1984).

66. A. Sandberg and W. Roberts, "Thermomechanical Processing of Microalloyed Austenite", A. J. De Ardo, G. A. Ratz and P. J. Wray, eds., TMS-AIME, Warrendale, PA, USA (1982), 405.

67. M. Umemoto, H. Ohtsuka and I. Tamura, Proc. Int. Conf. on the Physical Metallurgy of the Thermomechanical Processing of Steels and Other Metals (THERMEC '88), Tokyo, 2 (1988), 769.

68. R. K. Amin and F. B. Pickering, "Thermomechanical Processing of Microalloyed Austenite", A. J. De Ardo, G. A. Ratz and P. J. Wray, eds., TMS-AIME, Warrendale, PA, USA (1982), 377.

69. E. Essadiqi, Ph.D. Thesis, McGill University, Montreal, (1986).

70. E. Essadiqi and J. J. Jonas, Metall. Trans. A, 20A (1989), 987.

71. E. Essadiqi and J. J. Jonas, Metall. Trans. A, 19A (1988), 417.

72. R. Pandi, M. Eng. Thesis, McGill University, Montreal, (1993).

73. R. Pandi and S. Yue, Trans. Iron and Steel Inst. Jpn., 34 No. 3 (1994), 270.

74. J. Z. Briggs and R. Q. Barr, High Temp. High Press., 3 (1971), 363.

75. R. W. Burman, J. Met., 29 (1977), 12.

76. A. Zarei-Hanzaki, Ph.D. Thesis, McGill University, Montreal, (1994).

77. A. M. Guillet, Ph.D. Thesis, McGill University, Montreal, (1990)

78. A. Trudel, M. Eng. Thesis, McGill University, Montreal, (1995).

79. M. G. Akben, Ph.D. Thesis, McGill University, Montreal, (1975).

80. ASTM Standard E-8M (1984), 146.

81. B. Sundman et al., Calphad, Royal Institution of Technology, Stockholm, 9 (1985), 150.

82. G. I. S. L. Cardoso, B. Mintz and S. Yue, Ironmaking and Steelmaking, 22 No. 5 (1995), 365.

83. G. F. Vander Voort, "Metallography Principles and Practice", McGraw-Hill (1984).

84. ASTM Standard E-112-85, 277.

85. J. I. Goldstein (Editor), "Scanning Electron Microscopy and X-Ray Microanalysis", Plenum Press, New York (1992).

86. E. B. Hawbolt, B. Chau and J. K. Brimacombe, Metall. Trans., 14A (1983), 1803.

87. E. B. Hawbolt, B. Chau and J. K. Brimacombe, Metall. Trans., 16A (1985), 565.

88. T. Maki, T, Nagamichi, N. Abe and I. Tamura, Tetsu-to-Hagane (J. Iron Steel Inst. Jpn.), 71 (1985), 1367.

89. D. McLean, "Grain Boundaries in Metals", Wiley, New York (1957).

90. B. Bay and N. Hansen, "Deformation of Polycrystals: Mechanisms and Microstructures", N Hansen et al. Eds., Risø National Laboratory, Roskilde, Denmark (1981), 137-144.

91. G. E. Dieter, "Mechanical Metallurgy", Third Edition, McGraw-Hill (1986).

Appendix I

MTS BASIC Compression Testing Control Program

```
10 REM
20 REM---CONSTANT TRUE STRAIN RATE INTERRUPTED
COMPRESSION TEST----
30 REM
40 REM**********PROGRAMED BY ABBASS ZAREI
HANZAKI**********
50 REM
60 REM
70 ERASE
80 DIM X(50,1),Y(50,1)
90 COMMON A(450,2),C(450,2),D(450,2),Z(450)
95 COMMON F(15)
100 COMMON H0,A0,D1,D2,D5,B,S0,I1,I2,D
110 COMMON C1,S1,S2,L0,A,J,N$,M$,T$
120 PRINT "SAMPLE IDENTIFICATION"; \ INPUT N$
130 PRINT \ PRINT "MATERIAL"; \ INPUT M$
140 PRINT \ PRINT "TEST TEMPERATURE"; \ INPUT T$
150 PRINT \ PRINT "INITIAL HEIGTH (mm)"; \ INPUT H0
160 PRINT \ PRINT "INITIAL DIAMETER (mm)"; \ INPUT D0 \
A0=PI*(D0)^2/4
```

```
170 PRINT \ PRINT "NUMBER OF DEFORMATIONS:"; \ INPUT D5
180 PRINT \ PRINT "FIRST DEFORMATION"; \ INPUT D1
190 IF D5=1 THEN GO TO 210
200 PRINT \ PRINT "SECOND DEFORMATION"; \ INPUT D2
210 PRINT \ PRINT "STRAIN RATE (1/s))"; \ INPUT S1
220 PRINT \ PRINT "TIME INTERPASS (s)"; \ INPUT T
230 PRINT \ PRINT "LOAD RANGE (kip)"; \ INPUT L \ L0=L*4.4482*1000
240 PRINT \ PRINT "STROKE RANGE (mm)"; \ INPUT S0
245 PRINT \ PRINT "HOW MANY DATA DO YOU NEED ?"; \ INPUT D
250 ERASE
255 GTIME(,M,H)
260 PRINT "DATE                :"; \ PRINT DAT$
265 PRINT "TIME                :"; \ PRINT H;":"M
266 PRINT
270 PRINT "************************ EXPERIMENTAL DATA
**************************"
280 PRINT \ PRINT
290 PRINT "FILE NAME           :"; \ PRINT N$
300 PRINT "MATERIAL            :"; \ PRINT M$
310 PRINT
320 PRINT "TEST TEMPERATURE    :"; \ PRINT T$
330 PRINT "INITIAL HEIGTH      :"; \ PRINT H0; \ PRINT "  (mm)"
340 PRINT "INITIAL DIAMETER    :"; \ PRINT D0; \ PRINT "  (mm)"
350 PRINT
360 PRINT "NUMBER OF DEFORMATION  :"; \ PRINT D5
365 PRINT "NUMBER OF REQUESTED DATA:"; \ PRINT D
370 PRINT
380 PRINT "FIRST DEFORMATION   :"; \ PRINT D1
390 PRINT "SECOND DEFORMATION  :"; \ PRINT D2
400 PRINT "STRAIN RATE         :"; \ PRINT S1; \ PRINT "  1/SEC"
410 PRINT "TIME INTERPASS      :"; \ PRINT T; \ PRINT "   SEC"
420 PRINT
```

```
425 PRINT "LOAD RANGE          :"; \ PRINT L; \ PRINT "   Kip"
430 PRINT "STROKE RANGE        :"; \ PRINT S0; \ PRINT "   (mm)"
440 W=SYS(4)
450 PRINT \ PRINT
460 PRINT "PRESS RETURN TO START THE TEST"; \ INPUT G$
470 PRINT \ PRINT
480 PRINT "STARTING THE AUTOMATIC POSITIONING OF THE
PISTON"
490 FGARB(1,"R", TIME 100,-.4)
500 ADIMMED(1,A)
510 FGGO
520 IF A<-3.00000E-03 THEN GO TO 540
530 GO TO 500
540 FGSTOP
550 S2=A*L0/A0
560 PRINT \ PRINT "THE STRESS ON THE SAMPLE IS: "; \ PRINT S2; \
PRINT "MPa"
570 ETIME \ SLEEP(1)
580 ADIMMED(3,B)
590 T1=D1/S1/50 \ T2=D2/S1/50
600 REM
610 FOR I=1 TO 50
620 H1=H0/EXP(D1*I/50)
630 X(I,0)=(H1-H0)/S0+B
640 NEXT I
650 REM
660 H2=H0/EXP(D1)+.254
670 H=(H0-H1)/S0
680 FOR I=1 TO 50
690 H3=H2/EXP(D2*I/50)
700 Y(I,0)=(H3-H2)/S0+.02+(B-H)
710 NEXT I
720 REM
```

```
722 T3=D1/S1
723 N3=T3/.025
724 T8=N3/D \ IF T8<1 THEN T8=1
725 T4=D2/S1
726 N4=T4/.025
727 T9=N4/D \ IF T9<1 THEN T9=1
729 REM ---- NOTE THAT TIME INTERVAL USED TO BE 0.05 RATHER
THAN 0.025 --
730 CKTIME(1,.025)
740 ADTIMED(1,A,,3,T8,1)
750 ADTIMED(2,A,,3,10000,1)
760 ADTIMED(3,A,,3,T9,1)
765 ADTRIGGER(3,F5,-1)
770 REM----------SET UP  THE SYSTEM----------
780 FGARB(1,"R", TIME T1, ARRAY X)
790 FGARB(1,"R", TIME 1.00000E-03,.02+(B-H))
800 PRINT \ PRINT "PRESS RETURN TO START THE DEFORMATION"; \
INPUT G$
810 ADINIT \ FGGO \ ADGO(1)
820 FGSTATUS(1,W) \ IF W<>0 THEN GO TO 820
830 ADSTOP(1)
840 REM
850 IF D5=1 THEN GO TO 910
860 ETIME \ SLEEP(T)
870 REM
890 FGARB(1,"R", TIME T2, ARRAY Y)
895 ADGO(3)
900 FGSTATUS(1,S) \ IF S<>0 THEN GO TO 900
910 ADSTOP \ FGSTOP \ CKSTOP
920 REM
930 FGIMMED(1,"R", TIME .5,0)
940 PRINT \ PRINT \ PRINT
950 PRINT "****** THE EXPERIMENT IS FINISHED******"; \ INPUT G$
```

```
960 FOR I=1 TO A
970 REM-----C1 IS THE MTS COMPLIANCE----------
980 C2=-ELEVEL(A(I,2))*L0
990 C1=.198769*(1-EXP(-1.15596E-07*C2^2))+2.00063E-05*C2
1000 Z(I)=H0+(ELEVEL(A(I,1))-B)*S0
1010 PRINT I,LOG(H0/Z(I))
1020 NEXT I
1030 PRINT \ PRINT
1031 X0=1.00000E-05
1032 FOR I=10 TO A
1033 X1=LOG(H0/Z(I))
1034 IF X1<X0 THEN 1037
1035 X0=X1
1036 NEXT I
1037 PRINT "I1=";I-1 \ I1=I-1
1038 FOR J=I TO A
1039 X2=LOG(H0/Z(J))
1040 IF X2>=X0 THEN 1042 \ X0=X2
1041 NEXT J
1042 I3=J
1043 G1=X0
1044 FOR I=I3 TO A
1045 G2=LOG(H0/Z(I))
1046 IF G2>(.2*G1) THEN 1048
1047 NEXT I
1048 PRINT "I2=";I+1 \ I2=I+1
1049 J=1
1070 FOR I=1 TO A
1080 IF I>I1 THEN IF I<I2 GO TO 1110
1090 D(J,1)=A(I,1) \ D(J,2)=A(I,2)
1100 J=J+1
1110 NEXT I
```

```
1120 REM
1130 ERASE
1140 PRINT \ PRINT
1150 PRINT "RESULTS FROM THE EXPERIMENT:"
1160 PRINT \ PRINT
1170 PRINT "INITIAL POSITION:"; \ PRINT B
1180 PRINT "TOTAL NUMBER OF DATA POINTS:"; \ PRINT J
1190 PRINT "NUMBER OF POINTS FOR THE FIRST DEFORMATION:"; \
PRINT I1
1195 F(0)=B \ F(1)=J \ F(2)=I1
1196 F(3)=I2 \ F(4)=H0 \ F(5)=D0 \ F(6)=D5 \ F(7)=D1 \ F(8)=S1
1197 F(9)=T \ F(10)=D2 \ F(11)=L \ F(12)=S0
1198 F(13)=B
1200 PRINT \ PRINT \ PRINT
1210 W=SYS(4)
1220 PRINT "DO YOU WANT TO SAVE THE DATA"; \ INPUT G$
1230 PRINT \ PRINT
1240 IF G$="N" THEN GO TO 1280
1250 OPEN "DU1:T"&N$ FOR OUTPUT AS FILE #1
1255 OPEN "DU1:K"&N$ FOR OUTPUT AS FILE #2
1260 FOUT(1,D(1,1),,0,F)
1265 FOUT(2,F(1),,0,F) \ CLOSE #2
1270 CLOSE #1
1280 PRINT \ PRINT "DO YOU WANT TO SEE THE DATA"; \ INPUT G$
1290 IF G$="N" THEN GO TO 1360
1300 OPEN "DU1:T"&N$ FOR INPUT AS FILE #1
1305 OPEN "DU1:K"&N$ FOR INPUT AS FILE #2
1310 FINP(1,C(1,1),,0,F) \ CLOSE #1
1315 FINP(2,F(1),,0,F) \ CLOSE #2
1320 FOR I=1 TO J
1325 PRINT I,
1330 PRINT ELEVEL(C(I,2))*L0/A0*H0/Z(I),
```

```
1340 PRINT Z(I),LOG(H0/Z(I))
1350 NEXT I
1355 PRINT "B=";F(13),"J=";F(1),"I1=";F(2)
1360 PRINT  \ PRINT "DO YOU WANT TO SEE THE GRAPHICS"; \ INPUT
F$
1370 IF F$="Y" THEN CHAIN "GRAF5.BAS" LINE 270
1380 END

Ready
```

Appendix II

BASIC Program Used to Generate MTS TestStar Playback File

```
10 PRINT "------------------------------------------------------------------------"
20 PRINT "Routine to produce end levels for MTS TestStar 'FILEPLAY'
procedure."
30 PRINT "  COMPRESSION: constant true strain rate"
40 PRINT "              by T. Maccagno "
50 PRINT "------------------------------------------------------------------------"
60 PRINT
70 PRINT "Enter the name of the MTS 'Fileplay' file"
80 INPUT "      (e.g. COM0-05.SFP ) "; FIL$
90 PRINT
100 PRINT "Enter the test parameters"
110 INPUT " No. of ramp segments for loading (e.g. 100) = "; NUMSEG
120 DIM LGTH(NUMSEG), ENDLVL(NUMSEG)
130 INPUT " Gauge length (mm) = "; LGTH(0)
140 INPUT " Max expected true strain = "; STMAX
150 INPUT " True strain rate (sec-1) = "; STRATE
160 TIMEINCR=STMAX/(STRATE*NUMSEG)
170 OPEN "O", #1, FIL$
180 PRINT#1, "   SHAPE=", "    ramp"
190 PRINT#1, "   Time", "    Level_Data1"
```

```
200 PRINT#1,
210 PRINT#1, "  sec", "   mm"
220 PRINT
230 PRINT " Time incr", " Endlevel", " Ramp rate"
240 PRINT "  (sec)", "   (mm)", "  (mm/min)"
250 FOR I=1 TO NUMSEG
260 LGTH(I)=LGTH(0)*EXP(-I/NUMSEG*STMAX)
270 ENDLVL(I)=LGTH(I)-LGTH(0)
280 RMPRATE=(LGTH(I)-LGTH(I-1))/TIMEINCR*60
290 PRINT USING " ###.###     "; TIMEINCR, ENDLVL(I), RMPRATE
300 PRINT#1, USING " ###.###     "; TIMEINCR, ENDLVL(I)
310 NEXT I
320 CLOSE #1
330 PRINT " Time incr", " Endlevel", " Ramp rate"
340 PRINT "  (sec)", "   (mm)", "  (mm/min)"
350 END
```